International Journal of Solids and Structures 94–95 (2016) 1–20

Contents lists available at ScienceDirect

International Journal of Solids and Structures

journal homepage: www.elsevier.com/locate/ijsolstr

Non-linear simulation of coiling accounting for roughness of contacts and multiplicative elastic-plastic behavior

Daniel Weisz-Patrault[a,*], Alain Ehrlacher[b], Nicolas Legrand[c]

[a] LMS, École Polytechnique, CNRS, Université Paris-Saclay, 91128 Palaiseau, France
[b] Laboratoire Navier, CNRS, École Ponts ParisTech, 6 & 8 Ave Blaise Pascal, 77455 Marne La Vallee, France
[c] ArcelorMittal Global Research & Development East Chicago 3001 East Columbus Drive, East Chicago, IN 46312, USA

ARTICLE INFO

Article history:
Received 1 October 2015
Revised 9 May 2016
Available online 20 May 2016

Keywords:
Coiling
Roughness
Contact
Multiplicative elasto-plasticity
Finite strains
Optimization

ABSTRACT

In this paper numerical simulations of coiling (winding of a steel strip on itself) and uncoiling are developed. Initial residual stress field is taken into account as well as roughness of contacts and elastic-plastic behavior at finite strains, considering the Tresca yield function and isotropic hardening. The main output is the residual stress field due to plastic deformations during the process. This enables to quantify additional flatness defects. The presented coiling simulation relies on a modeling strategy that consists in dividing each time step into two sub-steps. Each sub-step can be solved semi-analytically and numerical optimizations enable to obtain a general solution. Thus, reasonable computation times are reached and parametric studies can be performed in order to develop coiling strategies considering the process parameters. Comparisons with previous models from the literature are presented. Moreover, the comparison with a Finite Element simulation presents the same order of magnitude, however, it shows that direct computations using classical FE codes are difficult to perform in terms of computation times and stability if an explicit integration scheme is chosen. Numerical results are also given in order to determine the effect of some parameters such as roughness, yield stress, applied force, strip crown or mandrel's radius.

1. Introduction

The coiling process consists in winding under tension a steel strip on a cylindrical mandrel. This process is very commonly used for storage in the steel-making industry and takes place after two main processes namely the rolling process on the one hand where the strip thickness is reduced between two rotating rolls and the run out table on the other hand where a cooling path is imposed in order to reach a targeted micro-structure. A schematic view of these is presented in Fig. 1. Large heterogeneous plastic deformations and phase changes occur during these latter processes leading to significant residual stress issues. Residual stress profiles are called flatness defects because they are responsible for out of plane deformations when tension is released and the strip is cut. Flatness prediction is one of the major issue of the steel-making industry, thus many papers proposed numerical simulations of rolling process in order to improve knowledge of residual stresses as a function of rolling parameters. One can mention a review of numerical simulations of rolling process published by Montmitonnet (2006). Jiang and Tieu (2001) proposed a rigid plastic/visco-plastic FEM and Hacquin (1996) published a 3D thermo-mechanical strip/roll stack coupled model called LAM3/TEC3 developed by Cemef, Transvalor, ArcelorMittal Research and Alcan. Abdelkhalek et al. (2011) computed the post-bite buckling of the strip, which is added to the older simulation of Hacquin (1996). Nakhoul et al. (2014) used a coupled Finite Element Modeling in order to predict manifested flatness defects. The impact on flatness of heterogeneous temperature field on the one hand and friction on the other hand is investigated. Kpogan and Potier-Ferry (2014) developed a simplified numerical method in order to predict the response of long thin strips considering residual stresses. Nakhoul et al. (2015) developed a two-scaled buckling model to predict the occurrence and geometric characteristics of manifested flatness defects. Recently Cuong et al. (2015) published an experimental and numerical modeling of flatness defects. Furthermore inverse methods dedicated to experimental evaluation of contact conditions during the rolling process have been developed in order to offer an experimental counter-part to predictive models. For instance, Weisz-Patrault (2015) reviewed some flatness control procedures and proposed an inverse Cauchy method using conformal mapping techniques that evaluate the residual stress profile in the strip. In addition, Weisz-Patrault et al. (2011, 2013b) published fast inverse methods (in 2D and 3D) dedicated to contact

* Corresponding author. Tel.: +33652836283.
E-mail address: weisz@lms.polytechnique.fr (D. Weisz-Patrault).

http://dx.doi.org/10.1016/j.ijsolstr.2016.05.012
0020-7683/

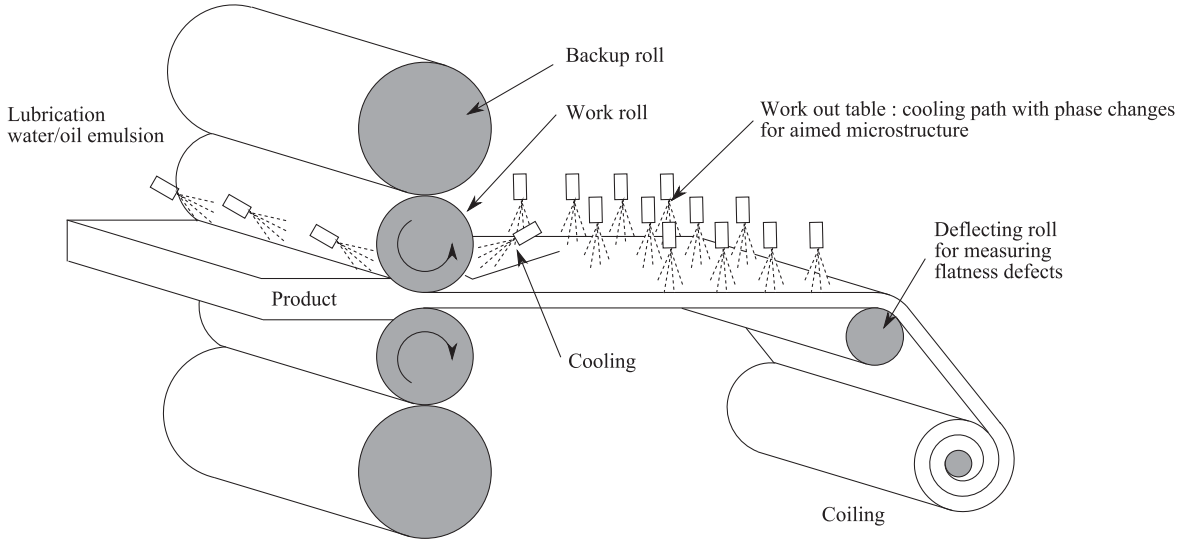

Fig. 1. Schematic view.

stress evaluation in the roll gap in real time during the rolling process. An experimental study based on this inverse method and optical fiber measurements has also been proposed by Weisz-Patrault et al. (2015b). Fast inverse methods have been developed for the thermal characterization of the contact between the strip and the work roll during the rolling process in 2D and 3D by Legrand et al. (2013); Weisz-Patrault et al. (2012a) and a thermo-elastic coupling have been published by Weisz-Patrault et al. (2013a). Experimental studies showing the feasibility of temperature measurements during the rolling process and performances of the associated inverse methods have been led by Legrand et al. (2012); Weisz-Patrault et al. (2014, 2012b).

Specific flatness defects occur during the coiling process as illustrated by Counhaye (2000). Indeed, for rather thick strips or small mandrels radii the curvature can generate significant plastic deformations. Furthermore, the geometrical strip profile of a cross section is not rectangular but more often parabolic, thus the strip center is thicker than the edges. Therefore the contact of the strip on itself is not ensured all along the coil width and a barrel shape is commonly observed. Usually the contact length decreases from the first layer to the last one and concentrates at the strip center (for parabolic geometrical profiles where the strip center is thicker). Consequently the contact pressure increases. This induces over-tension in the strip that is responsible for plastic deformations especially for the last layers where long center defects (or wavy center) are often observed because plastic elongations are localized at the center. Moreover, when large coils are obtained the first layers near the mandrel are submitted to large compressions that can also induce plastic deformations and short center defects (or wavy edges) are observed because plastic shrinkage is localized at the center. These defects are presented in Fig. 2. In addition, when the coil cools down phase changes occur modifying the residual stress distribution. Thus, modeling the coiling process is part of the general effort to predict flatness defects. There are several attempts to simulate effectively the winding of a strip on a mandrel.

Edwards and Boulton (2001) presented major issues related to the coiling process as well as an interesting review of the early models. For instance, soft or tight center collapses of coils are described on the basis of industrial experiences, however, the present contribution does not deal with such issues and focuses on numerical coil winding simulation. Most of coil winding models use thin or thick-walled elastic theory for hollow cylinders. Within this

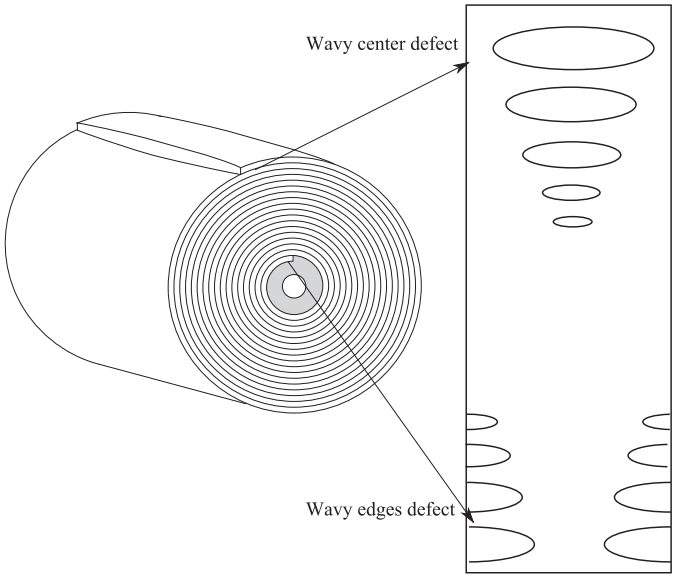

Fig. 2. Specific flatness defect.

frame work (Sims and Place, 1953) proposed an approach based on the theory of wire-winding of gun barrels. Based on experimental results, (Wilkening, 1965) emphasized that the model proposed by Sims and Place (1953) fails after 55 wound wraps, because stresses are widely overestimated. Altmann (1968) introduced an analytical solution considering constant radial Young's modulus, but tangential stress could not evolve. Wadsley and Edwards (1977) fixed the radial Young's modulus of the coil to a very low value compared with the standard value of the constituting material. This anisotropy is an attempt to model roughness of contacts. Thus, the coil is modeled as a hollow cylinder but the radial Young's modulus is decreased in order to take into account surfaces interpenetration due to roughness. However, the strip thickness variations are not taken into account. The model proposed by Edwards and Boulton (2001) also uses a radial Young's modulus that varies with the number of wound wraps. However, it seems that contact is imposed all along the coil width, no open gaps are formed between the wraps at any point. As detailed above, the contact length actually decreases because of the geometrical profile of the strip. It

is considered that results in zones where the contact is effectively ensured are not very affected by the assumption consisting in imposing contact all along the strip width. Hudzia et al. (1994) also developed a model (for which radial anisotropy has been added later) that takes into account the contact length evolution during the coil winding. However, the mid-plane radius is not inferred from the elastic non-linear problem but imposed a priori. Kedl (1992) proposed a model where wound wraps are computed as thick-walled cylinders on top of one another. The radial Young's modulus is set as a function of contact pressure in order to model roughness. Lee and Wickert (2002) proposed a two-dimensional Finite Element analysis. Ärölä and von Hertzen (2007) developed a Finite Element model in a total Lagrangian formulation. An hyperelastic, anisotropic and radially non-linear behavior is considered. Axial and radial displacements are accounted for. One can also mention the work of de Hoog et al. (2007) which consists in fixing the resulting stress in the coil and inferring by inverse method the winding tension profile. This study is based on hyperelastic non-linear material. Liu (2009) published a non-linear elastic model based on displacement formulation that takes into account radial displacement compatibility at both interfaces namely mandrel/coil and coil/last wound wrap. Hinton (2011); Hinton et al. (2011) developed a fast simplified coil winding model for wedge geometrical profile based on Airy function. The model is elastic and assumes that contact is ensured all along the strip width.

Previous models do not take into account the strip curvature, the coil winding being seen as a stack of cylindrical layers. Weisz-Patrault et al. (2015a) developed a very fast[1] elastic non-linear model that takes into account both curvature and contact pressure under tension. Moreover, initial residual stress profile is considered in order to account for previous rolling and run out table processes. Two types of non-linearity are identified, finite strains during the curvature phase on the one hand and perfect contact problem on the other hand. This model is based on the idea that for each time-step an infinitesimal strip portion is wound on the rest of the coil by following two distinct steps. The first step consists in imposing a simple curvature to the strip (whose mid-plane is initially flat). The trial radius of curvature is unknown. The second step consists in making contact between the curved infinitesimal strip portion and the rest of the coil underneath. Both substeps are fully analytical and an explicit relationship between the contact pressure varying along the coil width and the trial radius of curvature is obtained. Finally, displacements, strains and stresses due to both successive steps are computed as a function of the trial radius of curvature, thus the resultant force of tensions along the circumferential direction is calculated. The radius of curvature is then optimized so that the latter resultant force matches the force imposed by the user (actually a torque is applied and characterizes the applied force). Although this optimization is performed numerically, computation times are very short because each step is solved analytically. The main weaknesses of this model are:

- To rely on a purely elastic behavior, that does not enable to estimate precisely the irreversible plastic deformations (even though the yield criterion can be computed and projected on the yield surface) causing the evolution of residual stresses during the coiling process.
- To model perfect contacts (i.e., surfaces interpenetration is not allowed) avoiding roughness issues even though an extension considering anisotropic material with radial Young's modulus depending on the contact pressure could be developed.

This paper extends the ideas developed by Weisz-Patrault et al. (2015a). An elastic-plastic behavior is considered using the Tresca yield function with isotropic hardening. Roughness is introduced by allowing surfaces interpenetration as a function of contact pressure for each interface of the coil. A significant issue of the modeling strategy is to obtain satisfying computation times for both substeps (simple curvature of the infinitesimal strip portion on the one hand and contact with the rest of the coil on the other hand). The curvature involving large rotations an analytical solution at finite strains (multiplicative formalism) has been derived by Weisz-Patrault and Ehrlacher (2015) considering von Mises and Tresca yield functions, isotropic hardening and initial residual stress profile. In the following, the second sub-step, that consists in making contact between the infinitesimal strip portion and the rest of the coil, is solved semi-analytically considering the Tresca yield function and isotropic hardening. Then a global coil winding model is proposed and relies not only on both sub-steps but also on numerical optimization procedures. Indeed, contact pressures for all interfaces in the coil are determined as a function of the trial radius of curvature by numerical optimization. A relationship between surfaces interpenetration and the contact pressure representing the material roughness is used as a simple input. Indeed this contribution does not aim at developing any roughness model, but only extracts from the literature a simple contact law. A brief literature survey is addressed in Section 5. Finally the radius of curvature of the infinitesimal strip portion is also determined by minimizing the difference between the resultant tangential force in the infinitesimal strip portion and the applied force (known as a function of the applied torque). Thus displacement, stress and elastic and plastic strain fields are determined all along the coiling process and irreversible plastic deformations are precisely obtained. Residual stresses are finally inferred by developing a simple purely elastic uncoiling model.

The paper is organized as follows. In Section 2 a general description fixes notations, reference and actual configurations and makes explicit the assumptions and the general model strategy. The optimization problem that arises in determining contact pressure in the whole coil is broached in Section 2.3. The final optimization that enables to satisfy the weak boundary conditions (resultant forces) is detailed in Section 2.4. Then, practical solutions for both sub-steps are broached in Sections 3 and 4. At that point the global model needs a contact law that accounts for roughness, thus details and a brief literature survey concerning roughness models are given in Section 5. Some comparisons with existing models are presented in Section 6 showing the influence of plastic deformations (for different yield stresses). The influence of roughness is detailed in Section 7. Finally a very simple uncoiling model is proposed in Section 8 in order to compute the residual stress field after unwinding the strip and releasing tension. Some numerical tests showing the influence of coiling parameters such as applied force, strip crown and mandrel's radius are presented in Section 9. Conclusive remarks are addressed in order to discuss computation times and improvements.

2. General description

2.1. Preliminaries

The Cartesian basis is denoted by $(\boldsymbol{e_X}, \boldsymbol{e_Y}, \boldsymbol{e_Z})$ and the associated coordinates are (X, Y, Z). As shown in Fig. 3, the incoming strip in the reference configuration is modeled as a semi-infinite domain denoted by:

$$\Omega_0 = \left\{(X,Y,Z) \in \mathbb{R}^3, X \in [0,+\infty[, Y \in [-\delta(Z), \delta(Z)], Z \in [-L, L]\right\} \tag{1}$$

S_0 denotes the strip cross section in the reference configuration, which is assumed to be symmetrical with regard to $\boldsymbol{e_Z}$. Thus upper and lower surfaces are defined by a function of Z denoted by

[1] Since optimizations are used, computation times are not as short as the model developed by Hudzia et al. (1994).

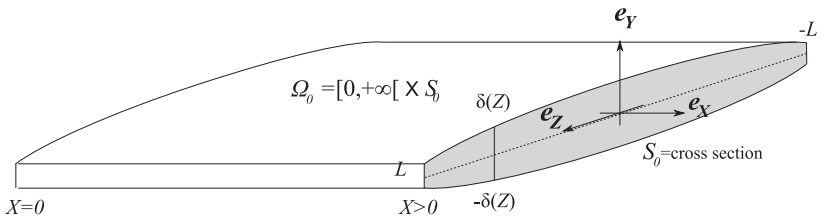

Fig. 3. Reference configuration.

Table 1
Nomenclature.

Ω_0	Semi-infinite domain
S_0	Cross section
$\boldsymbol{e_X}$, $\boldsymbol{e_Y}$, $\boldsymbol{e_Z}$	Cartesian basis
X, Y, Z	Cartesian coordinates (reference configuration)
$\delta(Z)$	Strip geometrical profile through thickness
L	Strip half-width
t_c	Strip thickness at the center
t_e	Strip thickness at the edges
R_{mand}^{ext}	External mandrel radius
R_{mand}^{int}	Internal mandrel radius
$\boldsymbol{e_r}$, $\boldsymbol{e_\theta}$, $\boldsymbol{e_z}$	Cylindrical basis
r, θ, z	Cylindrical coordinates (actual configuration)
k_0, μ_0	Bulk and shear moduli
σ_0	Initial yield stress
γ	Hardening parameter
$\underline{\boldsymbol{\Pi}}^{(0)}$	Residual stress tensor
$\underline{\boldsymbol{E}}^{(0)}$	Elastic tensor related to the residual stress
$J_0 = \det(\underline{\boldsymbol{E}}^{(0)})$	Determinant of the residual elastic tensor
$R^*(X)$	Trial radius of curvature
$R(X)$	Radius of curvature obtained by numerical optimization
$\boldsymbol{P}^*(X, Z)$	Trial vector of contact pressures in all interfaces
$\boldsymbol{P}(X, Z)$	Contact pressures obtained by numerical optimization
$[\![\boldsymbol{r_i}]\!](X, Z)$	Vector of surfaces interpenetration
$\underline{\boldsymbol{\sigma}}^{(1)}$	Cauchy stress tensor of step 1
$\underline{\boldsymbol{\sigma}}^{(2)}$	Cauchy stress tensor of step 2
$\underline{\boldsymbol{\sigma}} = \underline{\boldsymbol{\sigma}}^{(1)} + \underline{\boldsymbol{\sigma}}^{(2)}$	Cauchy stress tensor at the end of coiling
$F^*(X)$	Trial resultant tangential force
$F_a(X)$	Applied resultant tangential force
$\underline{\boldsymbol{\varepsilon}}^{p}$	Additional plastic strain tensor of step 2
$\boldsymbol{u}^{(2)}$	Displacement of step 2
$A([\![r_C]\!])$	Composite Abbott curve
$P_C = f([\![r_C]\!])$	Contact law
$\underline{\boldsymbol{E}}_0^u$	Elastic tensor before uncoiling
$\underline{\boldsymbol{\sigma}}^{u}$	Cauchy stress tensor before uncoiling
$\underline{\boldsymbol{E}}^{u}$	Elastic tensor after uncoiling
$\underline{\boldsymbol{\sigma}}^{res}$	Residual Cauchy stress tensor after uncoiling

$Z \mapsto \delta(Z)$. In the following, capital letters and the index zero indicate that the quantity is related to the reference configuration. All notations are listed in Table 1.

During the winding transformation, the observer is fixed to the mandrel. The latter does not rotate in this description and the strip wraps around the mandrel. Polar coordinates (r, θ, z) are used for the description of the actual configuration, as shown in Fig. 4. The rotation speed is denoted by ω so the already wound wraps are clearly defined by $\theta \in [0, -\omega t]$ and the remaining part is submitted to a rigid rotation. It should be noted that θ is negative and strictly decreasing when X is positive and strictly increasing.

Residual stresses are taken into account in this contribution. Indeed previous processes such as rolling process and run-out table are responsible for significant residual strains that are not compatible, thus an elastic field is needed so that the total deformation is compatible (i.e., is related to the gradient of a displacement field) leading to residual stresses. In this paper, it is assumed that the normal residual stress in the rolling direction is prevailing (all other normal stresses, including in-plane shear stresses are neglected). Moreover, this rolling-directed normal stress can vary throughout the strip. Thus, the residual stress tensor is denoted by $\underline{\boldsymbol{\Pi}}^{(0)} = \Pi_{XX}^{(0)}(X, Y, Z)\boldsymbol{e_X} \otimes \boldsymbol{e_X}$. The equilibrium is guaranteed, that is to say that over each cross section the resultant force of the residual stress profile vanishes.

The coiling process is fundamentally unsteady. However, this coil winding model relies essentially on a property similar to steady states: a unequivocal relationship between time and a space variable. Indeed, for each length of wound part there exists a unique corresponding time t. Therefore the time variable t can be substituted by a space variable denoted by $X_{max}(t)$, that represents the total length already wound. The infinitesimal strip portion considered in the following that lies between X and $X + \mathrm{d}X$ is taken for $X = X_{max}$ that is to say it is an infinitesimal strip portion being added to the coil at time t. So the already wound strip part is described by $X' \in [0, X = X_{max}]$.

2.2. Assumptions

The model relies on some assumptions specified here.

Assumption 1. Once in contact, slips are not allowed between wound wraps.

Assumption 2. Cross sections in the reference configuration ("X = Constant") are transformed in the actual configuration into cross sections ("θ = Constant").

Therefore, the angle representing the particle in the actual configuration depends only on X, more precisely the function θ: $X \mapsto \theta(X)$ is bijective. The assumption 1 enables to discard the time dependence and the assumption 2 enables to discard the Y and Z dependencies. Polar directions ($\boldsymbol{e_r}$, $\boldsymbol{e_\theta}$, $\boldsymbol{e_z}$) are obtained from ($\boldsymbol{e_X}$, $\boldsymbol{e_Y}$, $\boldsymbol{e_Z}$) (cf Fig. 4). An approximate transformation $\boldsymbol{\Phi}$ that describes the coiling process is sought. For sake of simplicity additional assumptions are needed:

Assumption 3. Plain strain assumption is made (planes "Z = Constant" in the reference configuration are transformed in the actual configuration into planes "z = Constant").

Thus, the transformation can be written as follows:

$$\boldsymbol{\Phi}(X, Y, Z, X_{max}) = r(X, Y, Z, X_{max})\boldsymbol{e_r} + Z\boldsymbol{e_Z} \tag{2}$$

Fields $r(X, Y, Z, X_{max})$ and $\theta(X)$ are unknown and should be determined. The X_{max} dependence (or equivalently the time dependence) in $r(X, Y, Z, X_{max})$ is due to the fact that when an arbitrary strip length is wound, the previous wound wraps are also deformed. Finally a very well verified assumption will be needed in this paper:

Assumption 4. The strip tension along the tangential direction $\boldsymbol{e_\theta}$ evolves very slowly with X (or equivalently with $\theta(X)$). Thus it is assumed that this tension profile is the same at X and at $X + \mathrm{d}X$.

Therefore, this model describes piecewise constant tension profile according to the rolling direction X. At each time step an infinitesimal strip portion is wound on the coil, the latter assumption ensures that computation does not depend on the discretization along X which is only a matter of choice in order to have several computed angular positions in the coil.

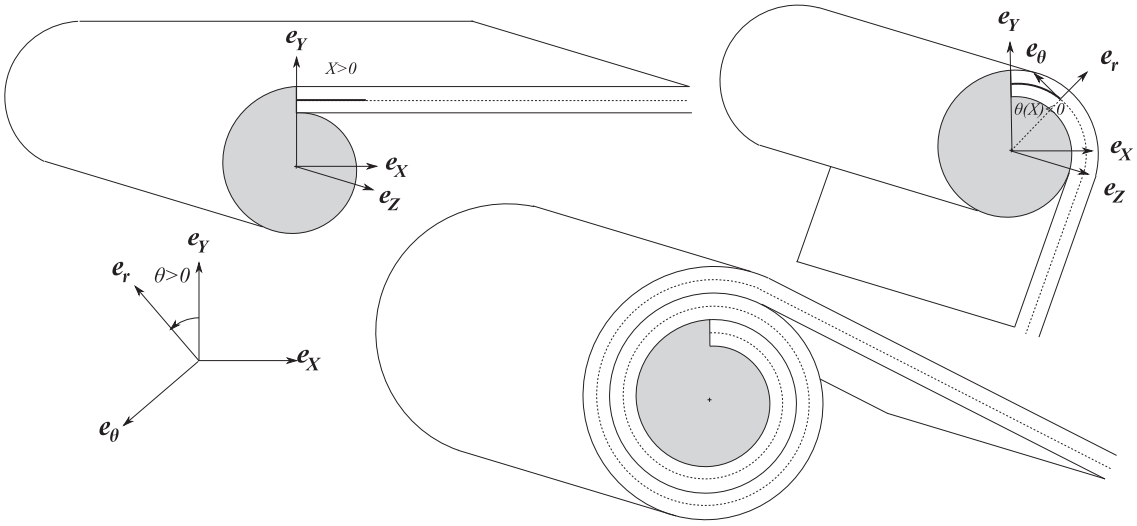

Fig. 4. Actual configuration : observer fixed to the mandrel.

2.3. Modeling steps

The modeling strategy is similar to the one developed by Weisz-Patrault et al. (2015a). At each time step an infinitesimal strip portion is wound on the coil. In order to obtain reasonable computation times each time step is subdivided into two distinct sub-steps that can be solved semi-analytically. It consists in applying a curvature transformation and then to put the curved infinitesimal strip portion in contact with the rest of the coil. Since the problem is non linear (contact problem, finite strain formalism and elastic-plastic behavior), the deformation path matters and other modeling choices could lead to different results. Thus, the decomposition into two successive sub-steps relies on the assumption that results would differ reasonably from one deformation path to another.

Step 1: The infinitesimal strip portion is curved arbitrarily with a trial radius of curvature $R^*(X)$ (Z-independent). Thus, this step corresponds to a global curvature of the strip portion regardless to the axial position Z, which will be corrected in step 2. The contact between the infinitesimal strip portion and the rest of the coil is not modeled during step 1. The trial radius $R^*(X)$ will be determined by applying weak boundary conditions in the end. This step involves large rotations and multiplicative elastic-plastic formalism is used. The mid-plane of the infinitesimal strip portion (initially flat) is transformed into a perfect cylinder of radius $R^*(X)$. More precisely the following transformation is imposed to the strip portion:

$$\boldsymbol{\Phi}^{(1)}(X,Y,Z) = (R^*(X)+Y)\boldsymbol{e_r} + Z\boldsymbol{e_Z} \tag{3}$$

where the superscript $^{(1)}$ refers to step 1. After the transformation $\boldsymbol{\Phi}^{(1)}$, the upper-plane has the radius $R^*(X)+\delta(Z)$ and the lower plane has the radius $R^*(X)-\delta(Z)$. This is obtained mostly by applying bending moments at both sections X and $X+\mathrm{d}X$. These bending moments are due to traction profiles through the strip thickness (i.e., $\boldsymbol{e_Y}$ direction). In the following, the associated Cauchy stress tensor $\underline{\boldsymbol{\sigma}}^{(1)}$ is evaluated as a function of the trial radius $R^*(X)$. In Fig. 5 this sub-step is summarized.

Since the transformation $\boldsymbol{\Phi}^{(1)}$ is imposed, unwanted body forces $\boldsymbol{f_b}$ are introduced and calculated with $\mathbf{div}\ \underline{\boldsymbol{\sigma}}^{(1)} = -\boldsymbol{f_b}$. However, the radial stress $\sigma_{rr}^{(1)}$ does not vanish at the upper and lower surfaces of the strip portion, and the resultant force of unwanted body forces compensates the unwanted resultant force of residual surface traction. Therefore, a global equilibrium is ensured through the strip portion thickness. This global equilibrium enables to use a simple transformation for modeling the curvature of the strip portion and is sufficient for the purpose of developing this simplified model. It should be mentioned that the radial Cauchy stress $\sigma_{rr}^{(1)}$ is not meaningful because of this global equilibrium instead of a local equilibrium, but the resultant through the strip thickness is meaningful. A schematic view of step 1 is presented in Fig. 5.

Step 2: The infinitesimal (curved) strip portion is put in contact with the rest of the coil. Contact pressures depend on the axial coordinate Z because of the geometrical strip profile. These contact pressures denoted by $\boldsymbol{P}^*(X,Z)$ are unknown and should be determined. An elastic-plastic model detailed in the following enables to compute the Cauchy stress tensor $\underline{\boldsymbol{\sigma}}^{(2)}$ (and all other quantities). Superscripts (1) and (2) are respectively related to step 1 and step 2. Furthermore, step 2 is an additive correction under infinitesimal strain assumption to the multiplicative computation at finite strains of step 1. Thus, the final state after both steps is written without superscript and for instance the final Cauchy stress is $\underline{\boldsymbol{\sigma}} = \underline{\boldsymbol{\sigma}}^{(1)} + \underline{\boldsymbol{\sigma}}^{(2)}$. Unlike the purely elastic model developed by Weisz-Patrault et al. (2015a) there is no analytical expression of the contact pressure as a function of the trial radius of curvature $R^*(X)$. However, contact pressures can be determined numerically for each value of $R^*(X)$. Moreover, in this contribution roughness is modeled as the possibility for each interface to interpenetrate each other via a contact law relating the contact pressure on the one hand and the interpenetration on the other hand. Thus, the rest of the coil cannot be modeled as a solid continuous medium (for axial positions where contact is ensured) like the previous paper of Weisz-Patrault et al. (2015a). In this paper, each contact should be up-dated at each time step where a new infinitesimal strip portion is added to the coil. Thus, the contact pressure $\boldsymbol{P}^*(X,Z)$ is not a scalar but a vector representing all contact pressures in the interfaces between all wound wraps (and also between the mandrel and the first wrap). A schematic view of step 2 is presented in Fig. 6.

Let $[\![\boldsymbol{r_i}]\!](X,Z)$ denote the vector containing interpenetration of all interfaces, defined as the radial position of the lower surface of the n-th wrap minus the radial position of the upper surface of the $(n-1)$th wrap. Thus, when a component of $[\![\boldsymbol{r_i}]\!](X,Z)$ is negative there is interpenetration at the corresponding interface, and there is no contact when it is sufficiently positive). The contact law is defined in each interface as follows:

$$P_C = f([\![r_C]\!]) \tag{4}$$

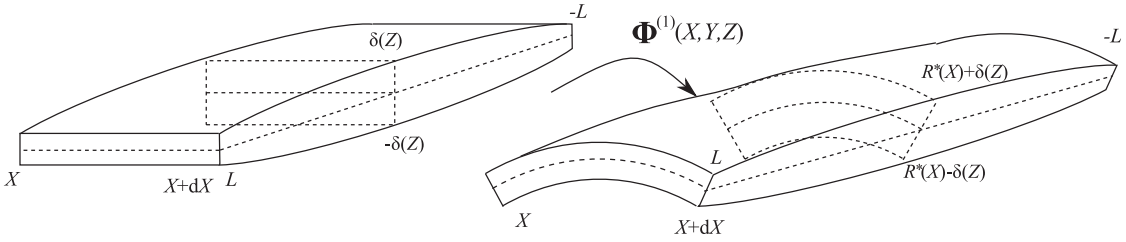

Fig. 5. *Step 1*: curvature.

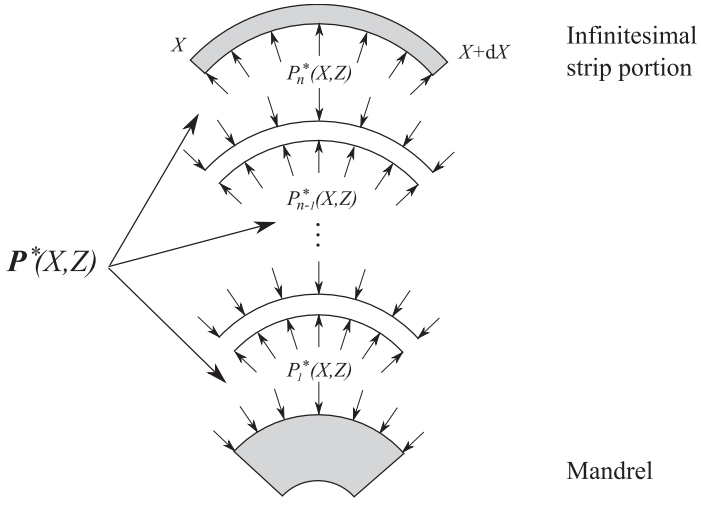

Fig. 6. *Step 2*: making contact.

where P_C denotes the contact pressure at the considered interface and $[\![r_C]\!]$ the interpenetration of surfaces. The function f is a characterization of the roughness and determined using classical literature (a proper survey is addressed in Section 5). Therefore, considering a trial value of $R^*(X)$, contact pressures are obtained by setting a trial value $\widetilde{\boldsymbol{P}}^*(X,Z)$ and computing the corresponding interpenetration $[\![\boldsymbol{r_i}]\!](X,Z)$ using the elastic-plastic model detailed in Section 4. Then, the contact law (4) is used for each interface and gives an other evaluation of contact pressures denoted by $\widetilde{\widetilde{\boldsymbol{P}}}^*(X,Z)$. Thus contact pressures corresponding to the trial value $R^*(X)$ are given by the optimization problem:

$$\forall R^*(X),\ \boldsymbol{P}^*(X,Z) = \underset{\widetilde{\boldsymbol{P}}^*(X,Z)\geq 0}{\operatorname{argmin}} \left| \widetilde{\boldsymbol{P}}^*(X,Z) - \widetilde{\widetilde{\boldsymbol{P}}}^*(X,Z) \right| \tag{5}$$

In order to be compared with other models that do not take into account roughness, perfect contacts without surfaces interpenetration are also implemented as an option. In that case, considering a trial value of $R^*(X)$, a trial value $\widetilde{\boldsymbol{P}}^*(X,Z)$ is set and the corresponding interpenetration $[\![\boldsymbol{r_i}]\!](X,Z)$ is computed using the elastic-plastic model detailed in Section 4. Then the following optimization ensuring that surfaces interpenetration vanishes is solved:

$$\forall R^*(X),\ \boldsymbol{P}^*(X,Z) = \underset{\widetilde{\boldsymbol{P}}^*(X,Z)\geq 0}{\operatorname{argmin}} |[\![\boldsymbol{r_i}]\!](X,Z)| \tag{6}$$

It should be noted that previous optimizations are done for each tested $R^*(X)$. Moreover, since all previous contacts are considered for each axial position, the number of parameters involved in latter optimizations is higher and higher. Thus, a significant issue is to reach very short computation times for the elastic-plastic problem of step 2. Semi-analytical solution has been developed to that end.

2.4. Weak boundary conditions

As mentioned in the introduction, a final optimization is needed in order to satisfy boundary conditions. A torque is applied to the mandrel, therefore a tangential force applied to the infinitesimal strip portion is inferred. It should be noted that the detailed tension profile through the strip thickness and width cannot be imposed and should be considered as an output. Therefore, the resultant force of tangential Cauchy stress in the infinitesimal strip portion denoted by $F^*(X)$ should match the applied force denoted by $F_a(X)$. Actually $F_a(X)$ is time dependent because the applied torque decreases during the coiling process in order to avoid overstretch since the tension profile tends to concentrate because of the evolution of the contact length. However, time can be replaced by a space variable as mentioned in Section 2.1. Boundary conditions are weak (because of the integration through strip thickness and width of the local stress field).

$$F^*(X) = \int_{-L}^{L}\int_{-\delta(Z)}^{\delta(Z)} \sigma_{\theta\theta}(X,Y,Z)\mathrm{d}Y\mathrm{d}Z \tag{7}$$

Thus the final optimization that determines the radius of curvature $R(X)$ solution of the winding problem is:

$$\forall X,\ R(X) = \underset{R^*(X)}{\operatorname{argmin}} |F^*(X) - F_a(X)| \tag{8}$$

Then, the contact pressure vector solution $\boldsymbol{P}(X,Z)$ is determined using (5), and all fields such as displacement, stress, elastic and plastic strains and hardening are determined through the elastic-plastic models of step 1 and step 2.

3. Elastic-plastic model of step 1

The elastic-plastic problem where the transformation (3) is imposed has been solved in details by Weisz-Patrault and Ehrlacher (2015). Multiplicative elastic-plastic behavior has been considered with isotropic hardening. All quantities such as the Cauchy stress

tensor, plastic strain etc... are computed straightforwardly. The solution relies on finding the only real root of a polynomial of degree three that can be calculated very effectively by using classical analytical solutions. However, considering the complexity of this analytical form, the elastic-plastic model of step 2 relies on interpolations of numerical results given by the present model of step 1 instead of a fully (and very extensive) analytical form. It has been emphasized by Weisz-Patrault and Ehrlacher (2015) that fields resulting from the present solution of step 1 are continuous but not differentiable (not smooth) at elastic/plastic interfaces. Therefore numerical results are interpolated by piece-wise polynomials of low degree (1 or 2) so that non differentiable points are not smoothed by the interpolation.

4. Elastic-plastic model of step 2

The elastic-plastic model of step 2 is an additive correction under infinitesimal strain assumption. In Fig. 6 it can be seen that a single model embraces all wound wraps. Since the *assumption 4* ensures that tension profiles are the same at both sections X and $X+\mathrm{d}X$ the model reduces to a cylindrical tube under plane strain assumption with inner and outer pressures considering prestress and the Tresca yield function. Many contributions focus on this kind of mechanical configuration because of its numerous engineering applications for vessels and piping for instance. Bree (1967) proposed an uni-axial elastic-plastic stress model in order to design nuclear reactor fuel elements. Then, Bree (1989) developed a bi-axial analytical solution for an elastic-plastic pressurized tube using the Tresca yield function and where stresses are averaged through the thickness. Gao (1993) developed an analytical solution based on one-dimensional elastic-plastic behavior of a closed end thick-walled cylinder. Chu (1972) proposed a numerical approach to solve an elastic-plastic pressurized thick-walled cylinder. Durban (1988) proposed a model at finite strains using finite logarithmic strains and neglecting elastic compressibility. Then, Durban and Kubi (1992) developed a more general analytical solution based on the Tresca yield function, however, considering the simple internal pressure loading only. One plastic mechanism and the corresponding corner solution are addressed. Bonn and Haupt (1995) proposed a solution for a thick-walled tube under internal pressure at finite strains based on the numerical approximation of elliptic partial differential equations. The autofrettage problem (i.e., generating residual stresses by plastic deformation and then shaping the thick walled cylinder by machining at the inner and outer surfaces) has been investigated by Parker (2001) (using numerical method) and Perry and Aboudi (2003) (using finite difference method). Several extensions of the initial thick-walled pressurized tube have been investigated. For instance Eraslan and Akis (2004) developed an analytical solution for a two-layers tube. Eraslan and Akis (2006) gave an analytical solution for a functionally graded elastic-plastic pressurized tube and Chatzigeorgiou et al. (2009) published an homogenization of a multilayer elastic-plastic pressurized tube with discontinuous material properties. Pronina (2013) developed an analytical solution of an elastic-plastic pressurized tube considering mechanochemical corrosion.

In this paper, a semi-analytical solution, for a thick-walled cylinder with inner and outer pressure and considering initial residual stress, is needed and derived in the following. In this section, for sake of clarity, polar coordinates (r,θ,z) are used and $r=R^*(X)+Y$. Moreover, the upper and lower surfaces of the wound wrap are respectively represented in the polar coordinates by $r=R_+$ and $r=R_-$. The imposed pressures at the upper and lower surfaces are respectively denoted by P_+ and P_-. Several mechanisms should be studied.

4.1. Elastic mechanism

The first possible mechanism is purely elastic (one can understand this calculation as an elastic test in order to check if the yield stress is exceeded). The elastic problem is computed analytically using for instance the complex formulas established by Muskhelishvili (1953):

$$\begin{cases} 2\mu_0 u_r^{(2)} = \dfrac{R_+^2R_-^2}{R_+^2-R_-^2}\left(\left(\dfrac{P_-}{R_+^2}-\dfrac{P_+}{R_-^2}\right)\dfrac{3\mu_0}{3k_0+\mu_0}r-\dfrac{P_+-P_-}{r}\right) \\ \sigma_{rr}^{(2)} = \dfrac{R_+^2R_-^2}{R_+^2-R_-^2}\left(\dfrac{P_-}{R_+^2}-\dfrac{P_+}{R_-^2}+\dfrac{P_+-P_-}{r^2}\right) \\ \sigma_{\theta\theta}^{(2)} = \dfrac{R_+^2R_-^2}{R_+^2-R_-^2}\left(\dfrac{P_-}{R_+^2}-\dfrac{P_+}{R_-^2}-\dfrac{P_+-P_-}{r^2}\right) \\ \sigma_{zz}^{(2)} = \dfrac{3k_0-2\mu_0}{2(3k_0+\mu_0)}\left(\sigma_{rr}^{(2)}+\sigma_{\theta\theta}^{(2)}\right) \end{cases} \tag{9}$$

Since $\sigma_{r\theta}^{(j)}=\sigma_{rz}^{(j)}=\sigma_{\theta z}^{(j)}=0$ principal stresses are $\sigma_{rr}^{(j)}$, $\sigma_{\theta\theta}^{(j)}$ and $\sigma_{zz}^{(j)}$ (where $j\in\{1,2\}$). Thus the Tresca yield function is written as follows:

$$Y_f = \max_{\alpha\in\{rr,\theta\theta,zz\}}\left(\sigma_\alpha^{(2)}+\sigma_\alpha^{(1)}\right)-\min_{\alpha\in\{rr,\theta\theta,zz\}}\left(\sigma_\alpha^{(2)}+\sigma_\alpha^{(1)}\right) -k(p_{cum}+\Delta p_{cum}) \tag{10}$$

where p_{cum} is the cumulative plastic strain calculated during step 1 according to Weisz-Patrault and Ehrlacher (2015) and Δp_{cum} is the increment of the cumulative plastic strain calculated during step 2, thus at the beginning of step 2, $\Delta p_{cum}=0$. Furthermore it is assumed that the yield surface can be written as follows:

$$k(p_{cum}+\Delta p_{cum}) = k(p_{cum})+\sigma_0\gamma\,\Delta p_{cum} \tag{11}$$

The yield criterion computed using the elastic test (9) can be negative and therefore the solution is purely elastic and given by (9), but it can also be positive and therefore plastic transformations occur. Several plastic mechanisms can be distinguished depending on which components of the principal stresses are the max and the min involved in (10). There are six possible plastic mechanisms corresponding to the six edges of the Tresca hexagon:

$$\max_{\alpha\in\{rr,\theta\theta,zz\}}\left(\sigma_\alpha^{(2)}+\sigma_\alpha^{(1)}\right)-\min_{\alpha\in\{rr,\theta\theta,zz\}}\left(\sigma_\alpha^{(2)}+\sigma_\alpha^{(1)}\right) = \begin{cases} \sigma_{\theta\theta}^{(2)}+\sigma_{\theta\theta}^{(1)}-(\sigma_{rr}^{(2)}+\sigma_{rr}^{(1)}) & \text{(mechanism 1)} \\ \sigma_{rr}^{(2)}+\sigma_{rr}^{(1)}-(\sigma_{\theta\theta}^{(2)}+\sigma_{\theta\theta}^{(1)}) & \text{(mechanism 2)} \\ \sigma_{\theta\theta}^{(2)}+\sigma_{\theta\theta}^{(1)}-(\sigma_{zz}^{(2)}+\sigma_{zz}^{(1)}) & \text{(mechanism 3)} \\ \sigma_{zz}^{(2)}+\sigma_{zz}^{(1)}-(\sigma_{\theta\theta}^{(2)}+\sigma_{\theta\theta}^{(1)}) & \text{(mechanism 4)} \\ \sigma_{rr}^{(2)}+\sigma_{rr}^{(1)}-(\sigma_{zz}^{(2)}+\sigma_{zz}^{(1)}) & \text{(mechanism 5)} \\ \sigma_{zz}^{(2)}+\sigma_{zz}^{(1)}-(\sigma_{rr}^{(2)}+\sigma_{rr}^{(1)}) & \text{(mechanism 6)} \end{cases} \tag{12}$$

The main activated plastic mechanisms are the first and the second. Thus in a plastic zone defined by $r=r_-^p$ and $r=r_+^p$, an analytical solution is derived for this mechanism. Boundaries of each plastic zone are unknown and should be determined in order to verify displacement and traction continuity through elastic/plastic interfaces. The evaluation of the yield function (10) on the basis of the elastic test (9) indicates the presence of a plastic zone where a particular mechanism is activated, but not the precise boundaries (usually obtained with incremental computations).

4.2. Plastic mechanisms 1 and 2

In this paper, plastic mechanisms 3 to 6 are not detailed although there are no particular difficulties to address an analytical solution. It is verified during the computation on the basis of

the elastic formulas (9) that these plastic mechanisms are not activated. The following piece-wise polynomials interpolation is used:

$$\chi k(r) - \left(\sigma_{\theta\theta}^{(1)} - \sigma_{rr}^{(1)}\right) = \sum_{j=0}^{N} A_j r^j \tag{13}$$

where A_j is piece-wise constant according to r and $\chi = 1$ if the mechanism 1 is activated and $\chi = -1$ if the mechanism 2 is activated. The detailed analytical solution is addressed in Appendix A. Here only the final result is stated:

$$\begin{cases} \varepsilon_{\theta\theta}^{p} = \dfrac{\mathcal{B}}{r^2} + \xi \displaystyle\sum_{j=0}^{N} A_j r^j \\ \sigma_{rr}^{(2)} = \mathcal{A} + (1+\xi c)A_0 \ln(r) + (1+\xi c)\displaystyle\sum_{j=1}^{N} \frac{A_j r^j}{j} - c\frac{\mathcal{B}}{2r^2} \\ \sigma_{\theta\theta}^{(2)} = \mathcal{A} + (1+\xi c)A_0 + A_0(1+\xi c)\ln(r) \\ \qquad +(1+\xi c)\sum_{j=1}^{N} \dfrac{A_j(1+j)r^j}{j} + c\dfrac{\mathcal{B}}{2r^2} \\ \sigma_{zz}^{(2)} = \dfrac{3k_0 - 2\mu_0}{2(3k_0+\mu_0)}\left[2\mathcal{A} + (1+\xi c)A_0 + 2A_0(1+\xi c)\ln(r)\right. \\ \qquad \left. +(1+\xi c)\sum_{j=1}^{N} \dfrac{A_j(2+j)r^j}{j}\right] \\ u_r^{(2)} = \dfrac{\mathcal{C}}{r} + \dfrac{r}{2\left(k_0 + \frac{\mu_0}{3}\right)}\left[\mathcal{A} + A_0(1+\xi c)\ln(r)\right. \\ \qquad \left. +(1+\xi c)\sum_{j=1}^{N} \dfrac{A_j r^j}{j}\right] \end{cases} \tag{14}$$

where $c = \chi\sigma_0\gamma\zeta\sqrt{\frac{4}{3}}$, $\zeta = \pm 1$ depending on the sign of the plastic strain rate as detailed in Appendix A and ξ is defined in (A.17).

The analytical solution given for each possible plastic zone should be used for the global elastic-plastic problem where plastic zones should be determined. The elastic test is computed with (9) then the yield function (10) is evaluated on this basis. Plastic zones with identified plastic mechanisms (limited in this paper to 1 and 2) are approximated on the basis of this purely elastic calculation. Then, both boundaries of each plastic zones (r_+^p and r_-^p) are optimized in order to verify boundary conditions (inner and outer pressures) and displacement and normal traction continuities through each elastic/plastic interfaces. Plastic strains should also vanish at these elastic/plastic interfaces. The integration constants $\mathcal{A}$, $\mathcal{B}$ and $\mathcal{C}$ involved in (14) are also determined with these latter conditions. It should be noted that integration constants $\mathcal{A}$, $\mathcal{B}$ and $\mathcal{C}$ are also piece-wise constant according to r. Since each zone has two boundaries, displacement and normal traction continuities and plastic strain vanishing give six conditions. There are three integration constants and optimizations of the two boundaries r_+^p and r_-^p, therefore five conditions can be satisfied and the last condition is automatically verified because of the constitutive equations. It should be noted that if one boundary of the considered zone is R_+ or R_- normal traction continuity is simply replaced by the corresponding applied normal pressure $-P_+$ or $-P_-$.

The Tresca yield function is not differentiable at wedges of the hexagon, that is to say when the activated plastic mechanism meets another plastic mechanism. This is classically refereed to as corner plasticity. Therefore, the associated flow rule that imposes that the plastic strain rate is normal to the yield surface, should be understood at these non-differentiable points as the fact that the plastic strain rate lies in the sub-differential of the yield surface. In this paper, corner relations that determine the plastic strain rate direction when a corner is reached, are not developed. It is verified numerically during the simulation that corners are not reached during step 2.

5. Contact law

In Section 4 each wound wrap has been solved considering arbitrary normal pressure at lower and upper surfaces. Excepted at the upper surface of the infinitesimal strip portion where the pressure vanishes, all other contact pressures listed in $\boldsymbol{P}^*(X, Z)$ are still unknown and should be determined as functions of $R^*(X)$ using the methodology summarized by (5). Therefore a contact law (4) has to be chosen. A general literature survey is given by Antaluca (2005). A historical paper proposed by Greenwood and Williamson (1966) presents a probabilistic approach for elastic contacts and has been extended to elastic-plastic contacts by Chang et al. (1987). Then, Polycarpou and Etsion (1999) corrected the exponential approximation introduced to obtain an analytical solution. More recently, a non-statistical model based on a multiscale approach has been proposed by Jackson and Streator (2006). Several classical roughness studies propose a relationship between the average contact pressure and the contact ratio, for instance Wilson and Sheu (1988), Sutcliffe (1988) and Sheu and Wilson (1994) established explicit simple formulas. In this paper, the empirical equation proposed by Sheu and Wilson (1994) is used $P_C = \frac{2}{\sqrt{3}}\sigma_0 A(2.571 - A - A\ln(1-A))$, where P_C is the average contact pressure between both considered surfaces, A is the contact ratio and σ_0 is the yield stress.

Then, the contact ratio A is calculated as a function of the algebraic distance between nominal surfaces (denoted by $[\![r_C]\!]$) by means of composite Abbott curves $A([\![r_C]\!])$ that can be inferred from random geometrical rough surfaces. This approach is used by Collette et al. (2000) for the contact of two rough surfaces within the framework of roughness transfer in rolling process. This paper does not focus on roughness theories but extracts from classical literature a contact law taking into account roughness parameters. The method used in this paper follows the ideas of Collette et al. (2000). The composite Abbott curve between two wound wraps characterized by the interpenetration of their nominal surfaces is obtained as follows. Two geometrical profiles that characterize roughness (R_a in μm) of each surface are randomly generated and centered to zero (nominal surfaces are set to zero). The discretization can be refined since it is not correlated with the general numerical simulation presented in this paper, it is clearly a pre-computation. Then the geometrical profile of the upper surface is subtracted from the geometrical profile of the lower surface, this gives the algebraic distance denoted by $[\![h]\!]$ between both surfaces when nominal surfaces are at the same position. For each algebraic value $[\![r_C]\!]$ it then computed the proportion of points where $[\![h]\!]$ is greater or equal than $[\![r_C]\!]$ which represents the probability of having contact, that is to say the contact ratio $A([\![r_C]\!])$. Random geometrical profiles are illustrated in Fig. 7 for a roughness parameter $R_a = 5$ μm. The corresponding composite Abbott curve is presented in Fig. 8a. It should be noted that curves such as presented in Fig. 8b are pre-computed and interpolated by cubic splines during the coiling simulation. Finally the contact law (4) can be written as follows and is presented in Fig. 8b.

$$P_C = f([\![r_C]\!]) = \frac{2}{\sqrt{3}}\sigma_0 A([\![r_C]\!])[2.571 - A([\![r_C]\!]) - A([\![r_C]\!])\ln(1 - A([\![r_C]\!]))] \tag{15}$$

Thanks to the roughness model, The coiling model is able to predict the evolution of strip roughness due to coiling using the same approach as Collette et al. (2000). This completes some previous works such as those of Collette et al. (2000) that modeled roughness transfer evolution at the skin pass mill. Moreover, this possibility of roughness transfer evolution of the model is particularly interesting since coiling-uncoiling operations are present all along the steel processes.

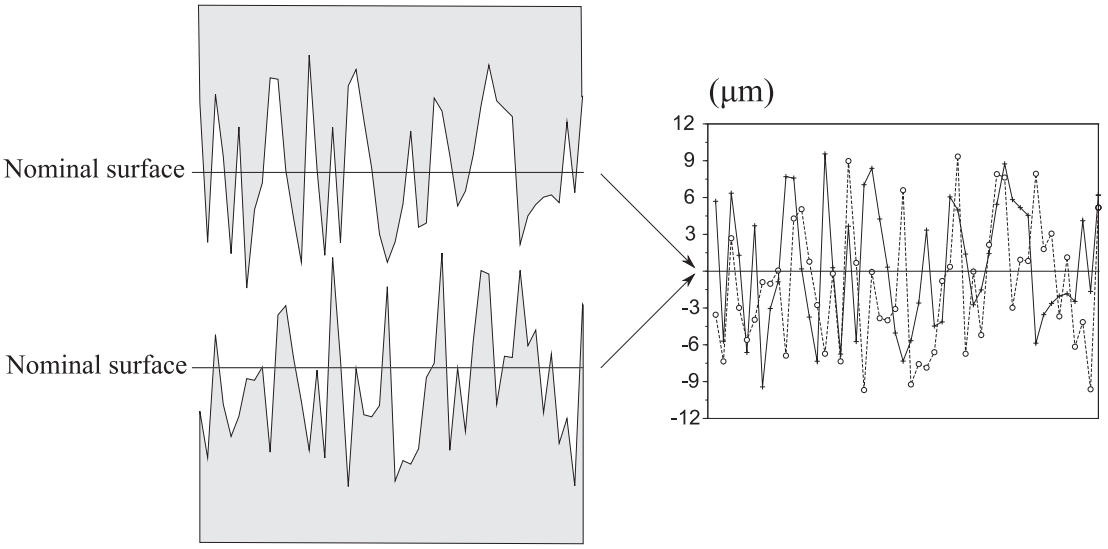

Fig. 7. Random geometrical profiles, $R_a = 5$ μm.

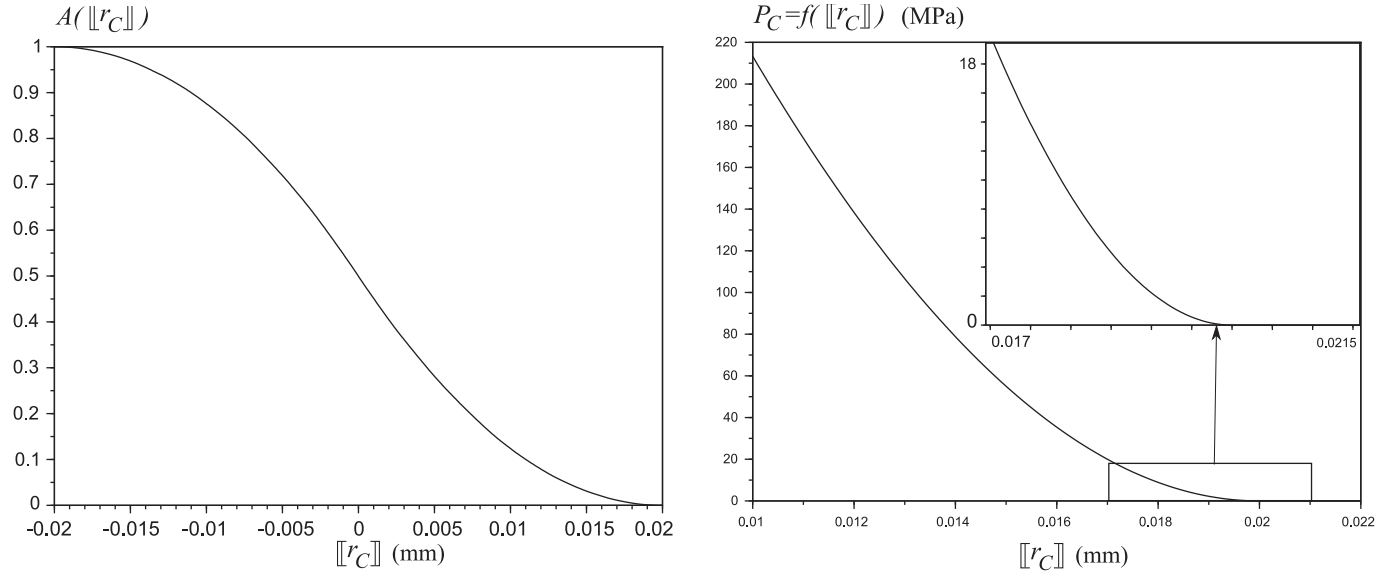

(a) Composite Abbott curve, $R_a = 5$ μm (b) Contact law, $R_a = 5$ μm

Fig. 8. Roughness.

6. Comparisons

6.1. Comparison with previous models and effect of yield stress

In this section, the present coiling model is compared with two purely elastic models developed by Hudzia et al. (1994) and Weisz-Patrault et al. (2015a). Typical coiling parameters are set and listed in Table 2. Roughness is not taken into account for this first comparison. A perfect contact is modeled using (6) instead of (5). The yield stress is $\sigma_0 = 200$ MPa for the present model. Contact pressures and tangential stresses at the mid-plane (i.e., $Y = 0$) are presented in Figs. 9a and 9b respectively. As mentioned in the introduction tensions are more and more concentrated at the center of the strip as shown in Fig. 9b. It can be seen that even though the model developed by Hudzia et al. (1994) considers the wrap radius as known a priori (strip thickness added to the previous radius), tangential stresses are in very good agreement with the purely

Table 2
Coiling parameters.

L	(mm)	750	Half-width
t_c	(mm)	1	Strip thickness at the center ($Z = 0$)
t_e	(mm)	0.952	Strip thickness at the edges ($Z = \pm L$)
$\delta(Z)$	(mm)	$\frac{1}{2}\left(t_c - (t_c - t_e)\left(\frac{Z}{L}\right)^2\right)$	Half thickness parabolic profile
R_{mand}^{ext}	(mm)	225	External mandrel radius
R_{mand}^{int}	(mm)	50	Internal mandrel radius
F_a/S_0	(MPa)	30	Applied force divided by the nominal surface (mean applied stress)
E	(MPa)	210000	Young's modulus
ν	(-)	0.3	Poisson ratio
k_0	(MPa)	175000	Bulk modulus
μ_0	(MPa)	80769.23	Shear modulus
γ	(-)	1	Hardening parameter

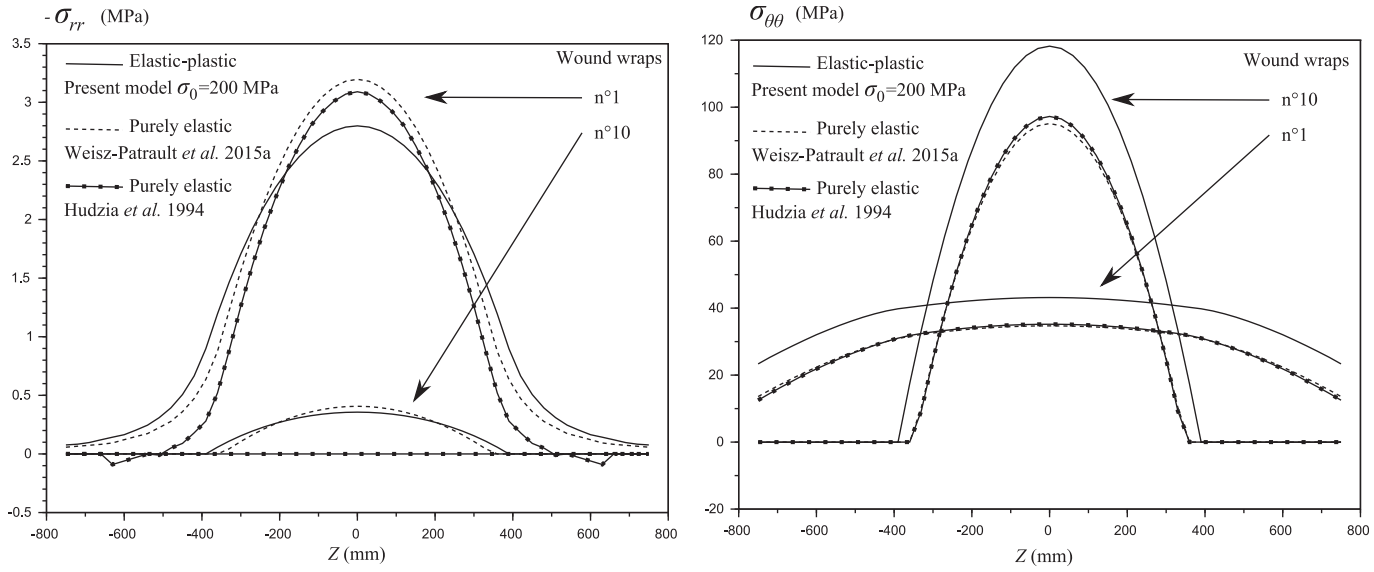

(a) Contact pressure, $-\sigma_{rr}$ (b) Tension at mid plane (i.e., $Y = 0$), $\sigma_{\theta\theta}$

Fig. 9. Comparison with the literature.

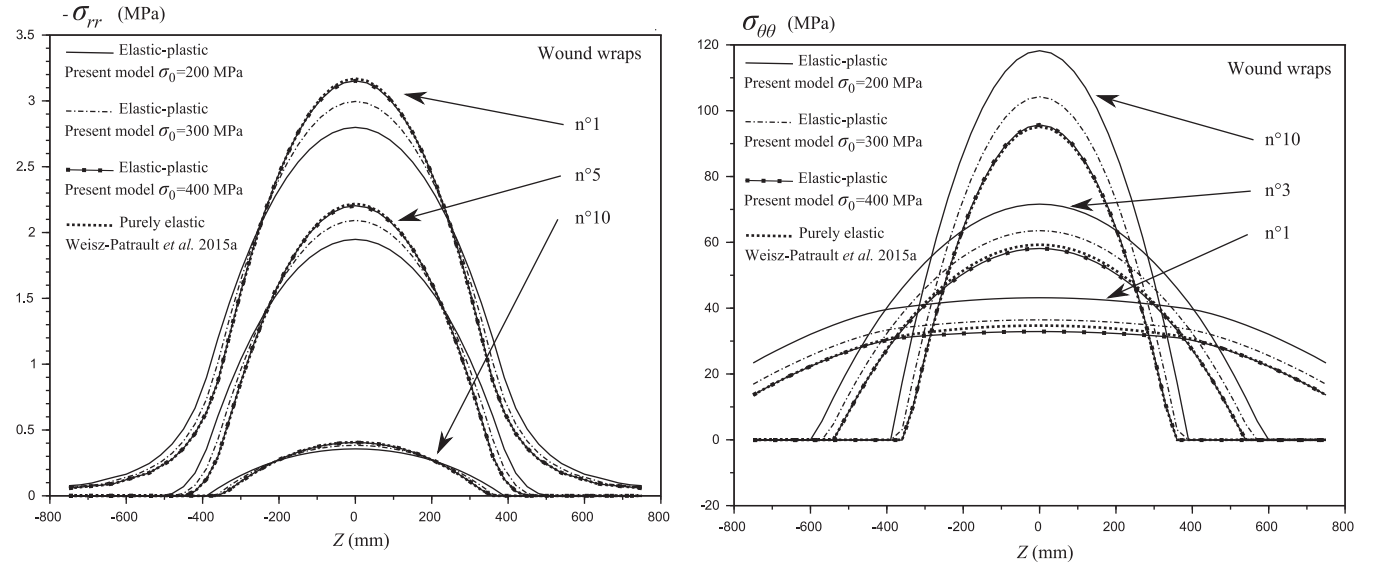

(a) Contact pressure, $-\sigma_{rr}$ (b) Tension at mid plane (i.e., $Y = 0$), $\sigma_{\theta\theta}$

Fig. 10. Different yield stresses.

elastic model developed by Weisz-Patrault et al. (2015a). It should be noted that negative contact stress σ_{rr} can be observed when contact is lost in the model proposed by Hudzia et al. (1994) which is excluded by construction in the present contribution and the one developed by Weisz-Patrault et al. (2015a). Since Hudzia et al. (1994) do not consider the strip curvature in the elastic computation models are only comparable at the mid-plane (i.e., $Y = 0$) where curvature effects vanish. However, contact pressures are not in excellent agreement with the previous model of Weisz-Patrault et al. (2015a). This is possibly due to the fact that (Hudzia et al., 1994) deals with the contact without using an explicit contact law and geometrical mismatch appears since each wrap radius is a priori known in order to have contact of thicker parts of wound wraps without considering displacements due to contact pressures. The present elastic-plastic model is in relatively good agreement with previous models. However, it can be noted for instance that the contact length of the first wound wrap is enlarged with the elastic-plastic behavior in comparison with the purely elastic behavior and stress magnitudes are modified. The effects of plasticity explain differences between the previous model of Weisz-Patrault et al. (2015a) and the present contribution as shown in Fig. 10 where several yield stresses from 200 MPa to 400 MPa have been compared with the purely elastic model in order to show that the elastic-plastic model converges to the elastic model when the yield stress increases. Furthermore, the lower the yield stress is and the lower the contact stress amplitude is. However, at mid-plane (i.e., $Y = 0$) this effect is inverted for tangential stress $\sigma_{\theta\theta}$. This is due to the fact that plastic flow concentrates near the upper surface of

Table 3
Coiling parameters, comparison with FEM.

L	(mm)	750	Half-width
t_c	(mm)	2	Strip thickness at the center ($Z=0$)
t_e	(mm)	1.94	Strip thickness at the edges ($Z=\pm L$)
$\delta(Z)$	(mm)	$\frac{1}{2}\left(t_c-(t_c-t_e)\left(\frac{Z}{L}\right)^2\right)$	Half thickness parabolic profile
R_{mand}^{ext}	(mm)	350	External mandrel radius
R_{mand}^{int}	(mm)	0	Internal mandrel radius
F_a/S_0	(MPa)	30	Applied force divided by the nominal surface (mean applied stress)
E	(MPa)	210000	Young's modulus
ν	(-)	0.3	Poisson ratio
k_0	(MPa)	175000	Bulk modulus
μ_0	(MPa)	80769.23	Shear modulus

each wrap which limits tangential stress in this plastic zone that is large when the yield stress is low. Thus, tangential stress is higher in the remaining elastic zone (especially at $Y=0$) in order to balance the applied force.

6.2. Comparison with Finite Element Model

A Finite Element model considering elastic-plastic behavior and hard contacts (i.e., without surface interpenetration) and performed with Abaqus (2006) was available from the previous paper of Weisz-Patrault et al. (2015a). A comparison with the model developed in this paper is presented in this section. The strip is modeled with cubic elements (20 along the axial direction Z, 750 along the coiling direction X and 3 along the strip thickness Y). The yield stress is set to $\sigma_0=200$ MPa and without hardening (i.e., $\gamma=0$) although Weisz-Patrault et al. (2015a) presented results for $\sigma_0=500$ MPa. Parameters are listed in Table 3. Considering very long computation times only 5 cycles have been modeled. Contact pressures that mostly determine stresses in each wound wrap are compared in Fig. 11. Contacts between layers are extracted from the FEM computation which excludes the contact between the first wrap and the mandrel (that is why the first wrap is missing in Fig. 11). Reasonable agreement is observed between the FEM computation and the developed model, however, discrepancies are not negligible. It should be noted that rather large oscillations and a clear lack of symmetry (although the problem is symmetric with respect to $Z=0$) lead to put in doubt the validity of this FEM computation. This can be due to the fact that only three elements are used through the thickness which may not be enough to evaluate properly displacements considering that plastic zones can be much thinner that elements thicknesses. In addition an explicit scheme has been chosen so that computation times are not excessively long and a lack of stability can also explain relatively bad results obtained with the FEM. Therefore contact pressures extracted from this FEM computation give only an order of magnitude.

7. Roughness

In this section roughness is taken into account considering the simple methodology proposed in Section 5. Parameters are listed in Table 2 with a yield stress set to $\sigma_0=600$ MPa (no significant plastic deformations) in order to see the effect of roughness only. Two computations have been done, the first one with perfect contacts and the second one considering roughness with $R_a=5$ μm. This value is not realistic and has been chosen in order to emphasize roughness effects after only 70 wraps. Contact pressures and tension at mid-plane (i.e., $Y=0$) after 10 wraps are presented in Figs. 12a and 12 b and after 70 wraps in Figs. 13a and 13 b. As mentioned in the introduction Wilkening (1965) gave experimental evidence that the model proposed by Sims and Place (1953) (purely elastic not taking into account roughness) overestimates stresses after 55 wound wraps. The model developed in this paper presents no significant discrepancies between perfect and rough contacts after 10 wraps. One can observe that the overestimation of contact pressure and tension when roughness is not taken into account becomes more substantial after 70 wraps. This confirms the significance of roughness.

One can also mention that tension of the first wrap in Fig. 13b locally decreases at the center. This is due to accumulation of pressure at the center. Indeed contacts are more and more localized

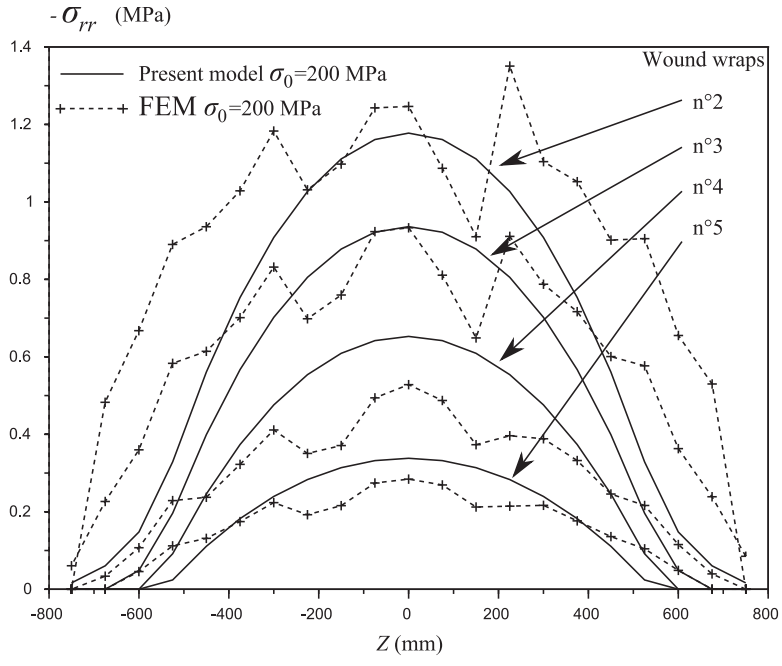

Fig. 11. Contact pressure, $-\sigma_{rr}$.

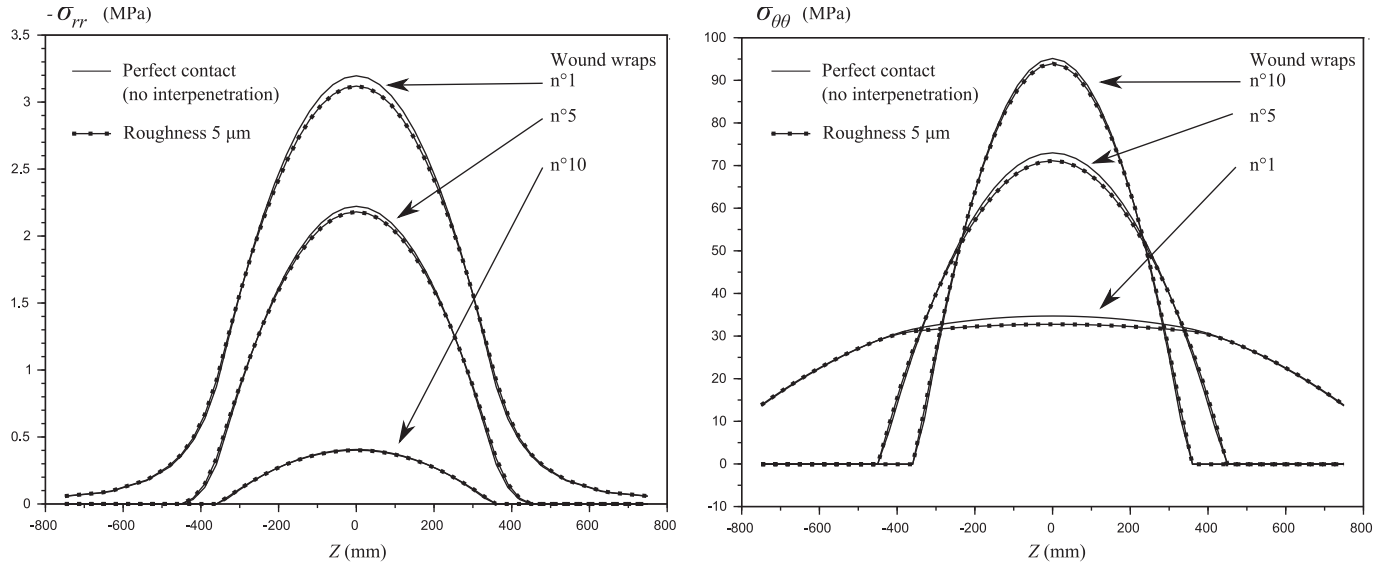

(a) Contact pressure, $-\sigma_{rr}$ (b) Tension at mid plane (i.e., $Y = 0$), $\sigma_{\theta\theta}$

Fig. 12. Effect of roughness after 10 wraps.

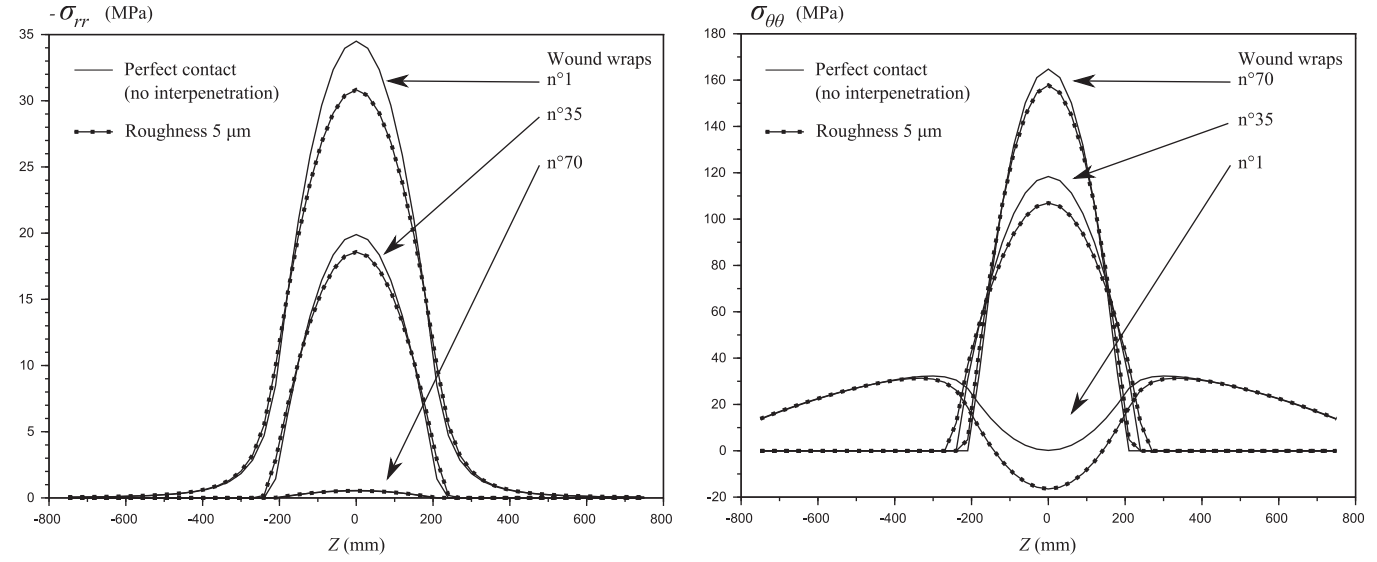

(a) Contact pressure, $-\sigma_{rr}$ (b) Tension at mid plane (i.e., $Y = 0$), $\sigma_{\theta\theta}$

Fig. 13. Effect of roughness after 70 wraps.

at the center, thus pressures increases where contacts localize, especially for the first wound wraps that are compressed by all the other wraps.

8. Residual stress : uncoiling model

As mentioned in the introduction, this paper aims at developing a numerical tool for evaluating residual stress field after coiling, in order to develop strategies to minimize flatness defects. Elastic-plastic computations have been developed in order to model the evolution of irreversible strain that causes residual stress after uncoiling. This section presents a very simplified residual stress computation that takes into account uncoiling, assuming that the latter process is purely elastic. It consists in making the strip mid-plane perfectly flat again. Obviously the strip is not perfectly flat after uncoiling because residual stresses are in fact relaxed by out of plane deformations. However, the interesting quantity is the residual stress profile when the strip mid-plane is perfectly flat in order to evaluate the flatness defect that will be created by this relaxation of residual stress including buckling analysis. This simple uncoiling calculation consist in releasing contact pressure by applying the opposite contact stress in all interfaces using the elastic formulas (9). At this stage the strip mid-plane is not a perfect cylinder because of the irreversible plastic deformations during step 2. A perfect cylinder is obtained by shifting the stress profiles through the strip thickness so that the elastic zone does not present residual stresses. The stress field $\underline{\underline{\sigma}}^u = \sigma^u_{rr}\boldsymbol{e_r}\otimes\boldsymbol{e_r} + \sigma^u_{\theta\theta}\boldsymbol{e_\theta}\otimes\boldsymbol{e_\theta} + \sigma^u_{zz}\boldsymbol{e_z}\otimes\boldsymbol{e_z}$ (where u means uncoiling) at the end of this step is the sum of the stress field at the end of coiling process and the stress field due to releasing contact pressures (computed with (9)) and

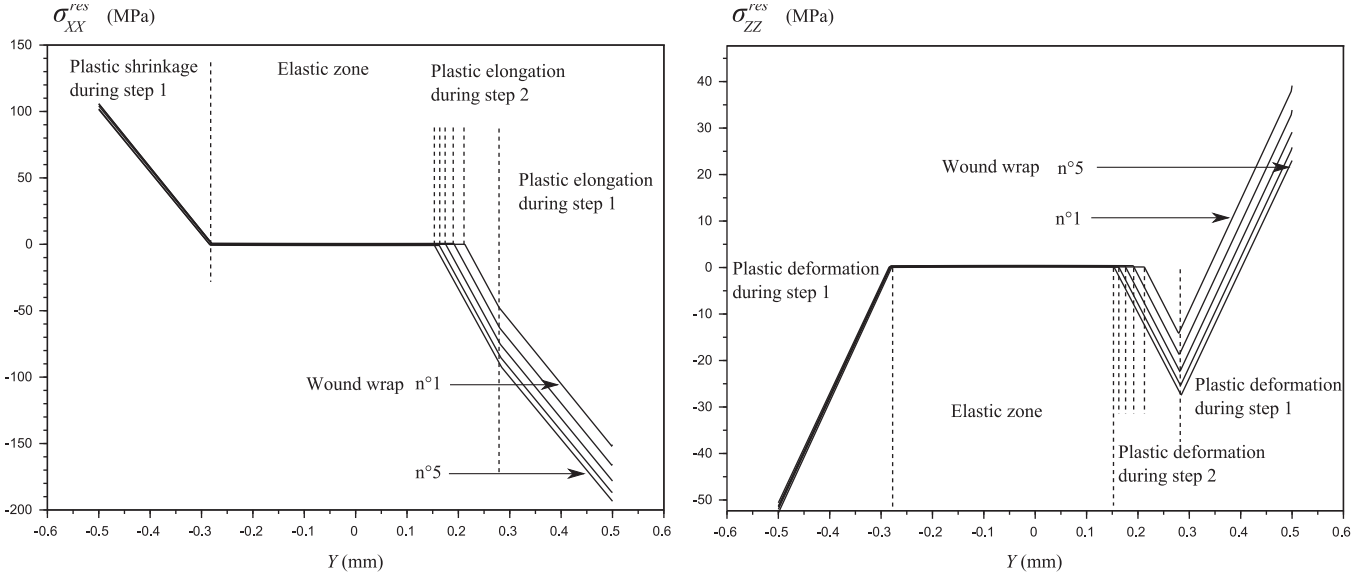

(a) Residual stress profiles σ_{XX}^{res} through thickness at $Z = 0$

(b) Residual stress profiles σ_{ZZ}^{res} through thickness at $Z = 0$

Fig. 14. Residual stress through the thickness.

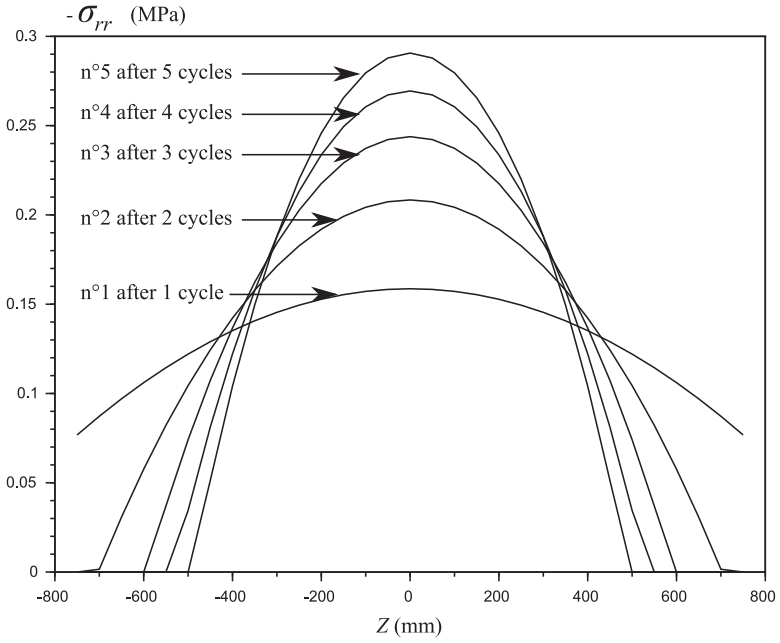

Fig. 15. Contact pressure, $-\sigma_{rr}$ for the last wrap.

considering the latter stress shift. It can be seen as an initial stress before applying the inverse transformation gradient corresponding to the curvature of step 1 defined by Weisz-Patrault and Ehrlacher (2015). This ensures that the mid-plane of the strip is flat. Thus, an elastic tensor is responsible for this stress field $\underline{\boldsymbol{\sigma}}^{u}$ and denoted by $\underline{\boldsymbol{E}}_0^u$ which is a diagonal tensor considering that the stress tensor is diagonal. One can obtain $\underline{\boldsymbol{E}}_0^u.{}^t\underline{\boldsymbol{E}}_0^u$ from the known stress field $\underline{\boldsymbol{\sigma}}^{u}$:

$$\underline{\boldsymbol{E}}_0^u.{}^t\underline{\boldsymbol{E}}_0^u = A_{rr}^u \boldsymbol{e_r}\otimes\boldsymbol{e_r} + A_{\theta\theta}^u \boldsymbol{e_\theta}\otimes\boldsymbol{e_\theta} + A_{zz}^u \boldsymbol{e_z}\otimes\boldsymbol{e_z} \tag{16}$$

where $(A_{rr}^u, A_{\theta\theta}^u, A_{zz}^u)$ are known functions determined as detailed in Appendix B. From the latter equation, the purely elastic uncoiling gives the residual stress field:

$$\begin{cases} \sigma_{XX}^{res} = \dfrac{\mu_0}{3\left(J_u\widetilde{J_u}\right)^{\frac{5}{3}}}\left(2\widetilde{J_u^2}A_{\theta\theta} - A_{rr} - A_{zz}\right) + k_0\left(J_u\widetilde{J_u} - 1\right) \\ \sigma_{YY}^{res} = \dfrac{\mu_0}{3\left(J_u\widetilde{J_u}\right)^{\frac{5}{3}}}\left(-\widetilde{J_u^2}A_{\theta\theta} + 2A_{rr} - A_{zz}\right) + k_0\left(J_u\widetilde{J_u} - 1\right) \\ \sigma_{ZZ}^{res} = \dfrac{\mu_0}{3\left(J_u\widetilde{J_u}\right)^{\frac{5}{3}}}\left(-\widetilde{J_u^2}A_{\theta\theta} - A_{rr} + 2A_{zz}\right) + k_0\left(J_u\widetilde{J_u} - 1\right) \end{cases} \tag{17}$$

where the superscript *res* means *residual*. For instance, considering coiling parameters listed in Table 2 where the applied force is set to $F_a/S_0 = 30$ MPa, the yield stress is $\sigma_0 = 200$ MPa and the

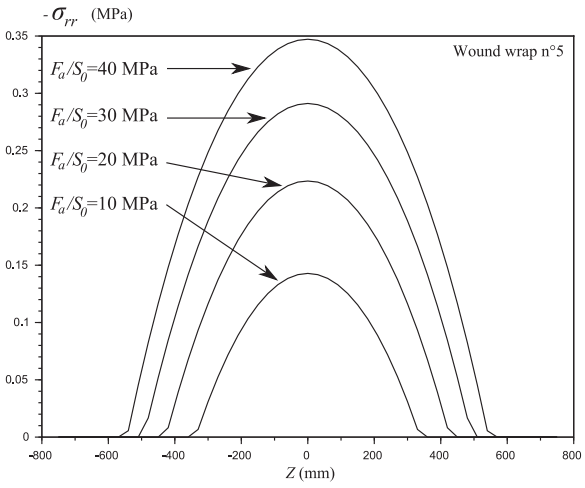

(a) Contact pressure for the 5th wound wrap

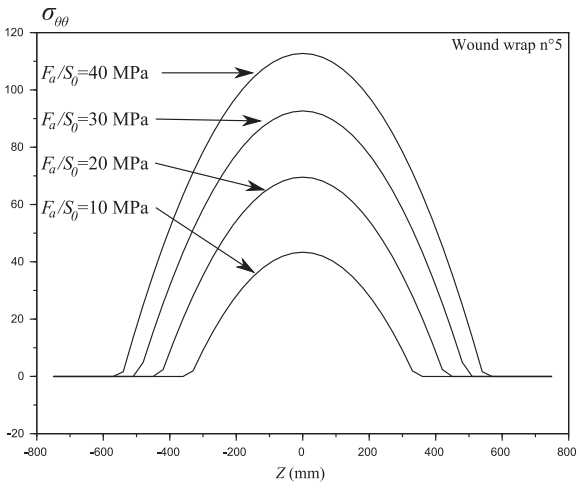

(b) Tangential stress for the 5th wound wrap

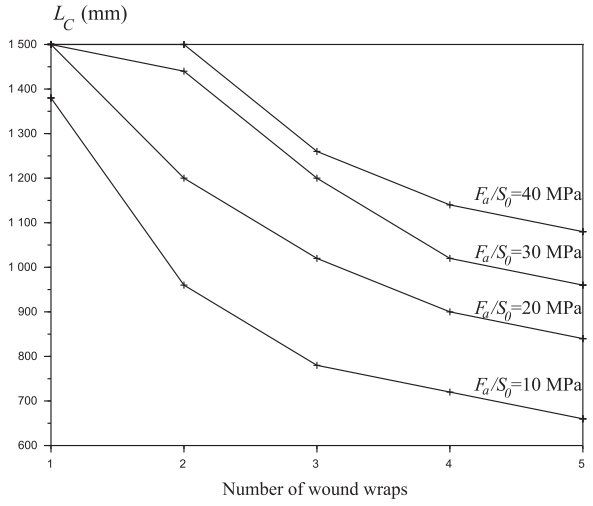

(c) Contact length

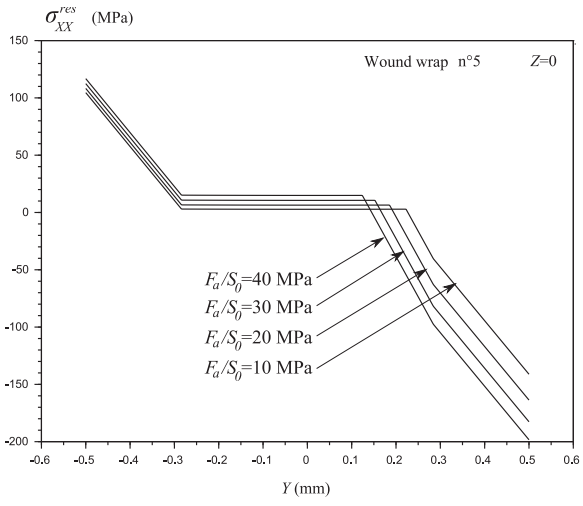

(d) Residual stress along thickness

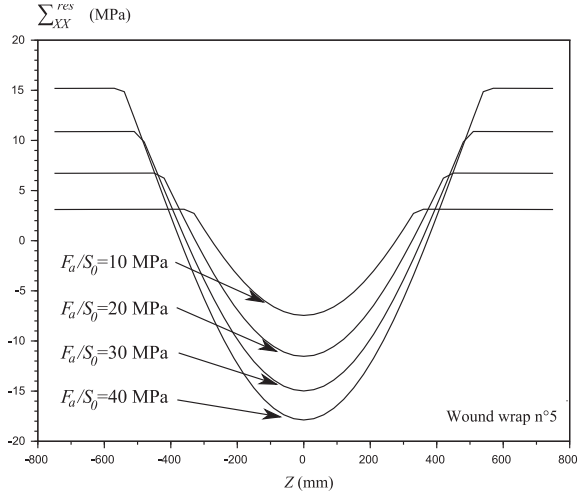

(e) Average residual stress along width

Fig. 16. Results for test 1.

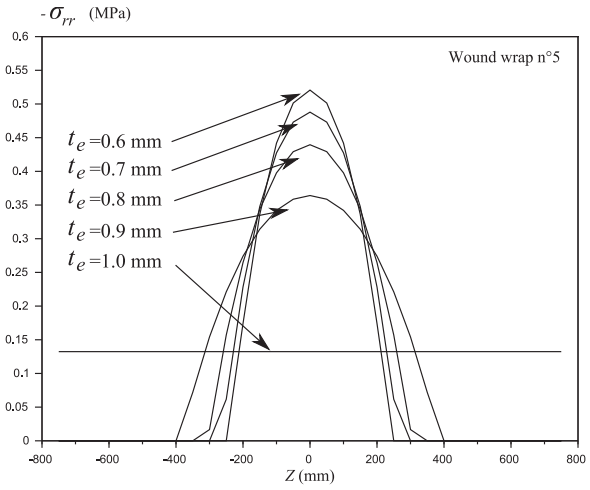

(a) Contact pressure for the 5th wound wrap

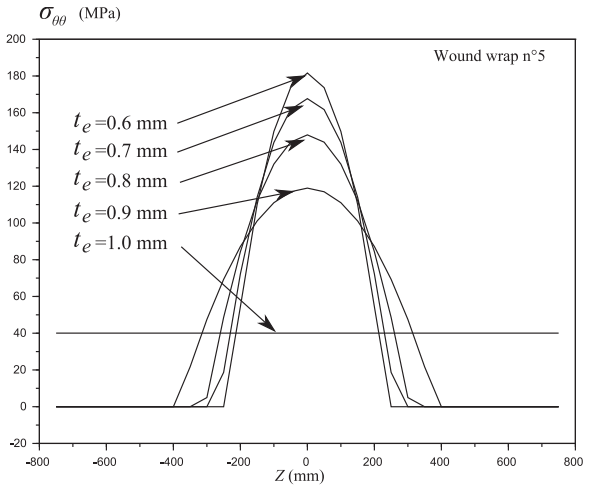

(b) Tangential stress for the 5th wound wrap

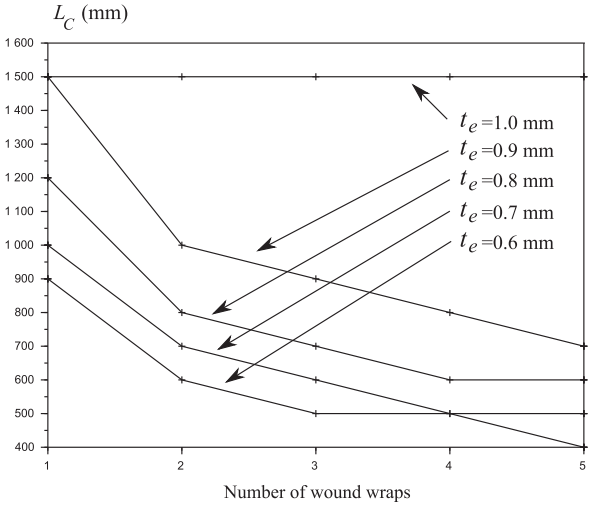

(c) Contact length

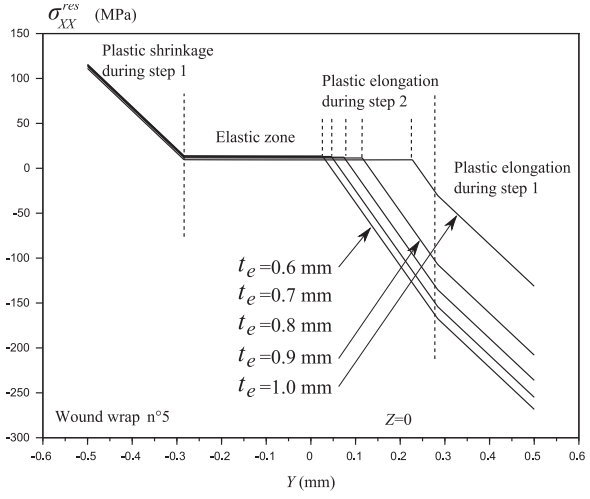

(d) Residual stress along thickness

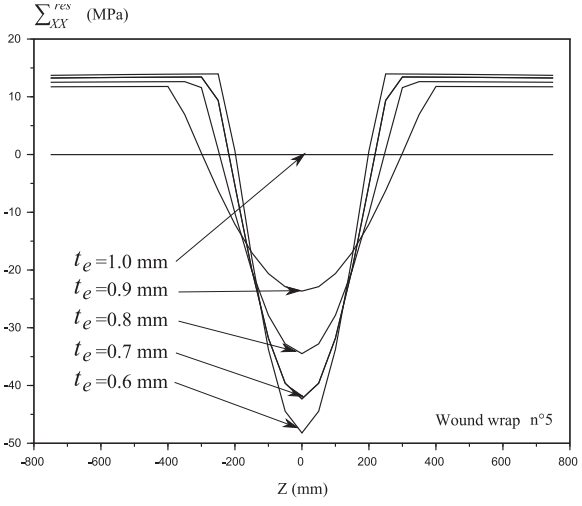

(e) Average residual stress along width

Fig. 17. Results for test 2.

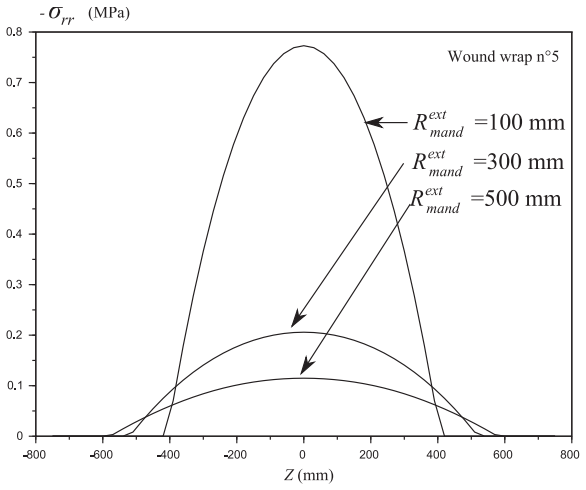

(a) Contact pressure for the 5th wound wrap

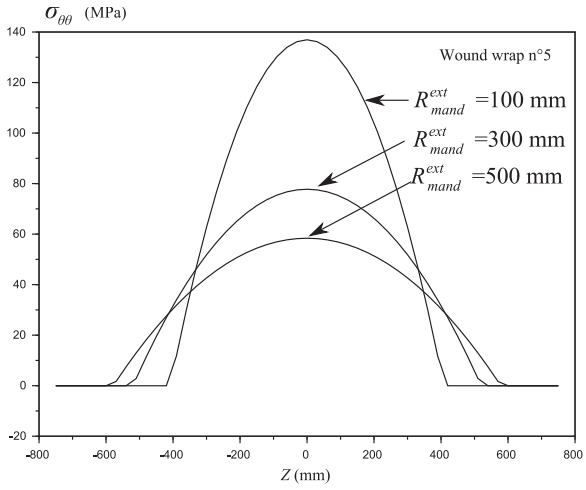

(b) Tangential stress for the 5th wound wrap

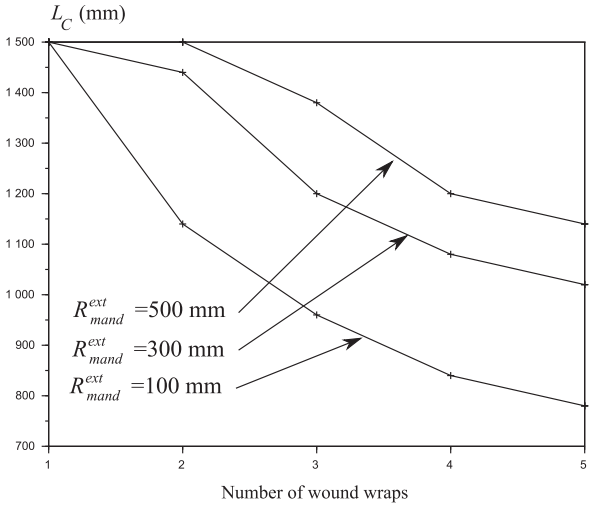

(c) Contact length

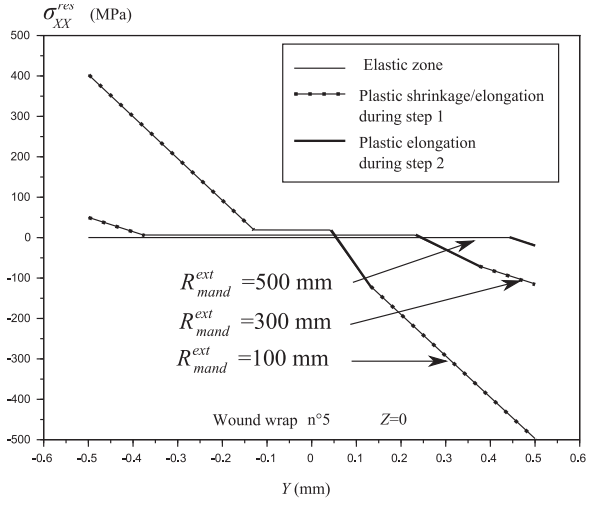

(d) Residual stress along thickness

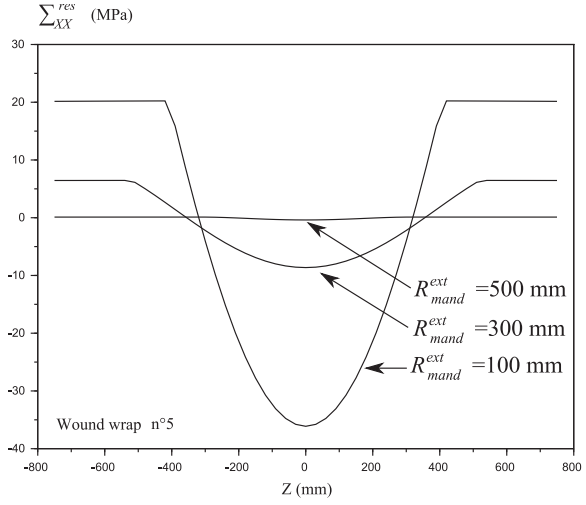

(e) Average residual stress along width

Fig. 18. Results for test 3.

Table 4
Varying parameters for each test.

(a) Test 1: Applied forces F_a/S_0 (MPa)
10
20
30
40
(b) Test 2: Strip profiles t_e (mm)
1
0.9
0.8
0.7
0.6
(c) Test 3: Mandrel's radii R^{ext}_{mand} (mm)
100
300
500

hardening parameter is $\gamma = 1$, it is obtained (ater 5 cycles) the residual stress profiles presented in Figs. 14a and 14b. Different zones are clearly identified with gradient discontinuities. These zones are indicated in Figs. 14a and 14b for the first wound wrap. During step 1 that consists in a simple curvature, the lower surface is under compression and the upper surface under tension that lead to plastic deformations. During step 2 contact pressure is applied and the whole thickness is under tension. Without step 1, this tension would not be sufficient to initiate plastic deformations however, since the upper surface is already under tension even very limited contact pressure is sufficient to lead to plastic deformations in a slightly thicker plastic zone. It should be noted that slope changes near the lower surface and upper surface are almost aligned for the five wound wraps. This is due to the fact that these slope changes correspond to plastic deformations during step 1 that are almost the same for these wound wraps (there is no significant variation of the radius of curvature $R(X)$). However, the slope change corresponding to plastic deformations during step 2 occurs more and more near the strip center (i.e., $Y = 0$) because contact pressure at $Z = 0$ localize as shown in Fig. 15. It should be noted that the latter figure presents the contact pressure at the lower surface of the wound wrap n after n cycles (contact pressure of the last wound wrap). This is different from previous figures such as 9a, 10a, [11,12]a, 13a where contact pressures for the wound wrap n are given after that all cycles are computed giving contact pressures in the whole final coil.

An interesting quantity (18) is the average residual profile calculated through the strip thickness and plotted along the coil width. This enables to understand major flatness defect as presented in Fig. 2.

$$\Sigma^{res}_{XX}(Z) = \frac{1}{2\delta(Z)} \int_{-\delta(Z)}^{\delta(Z)} \sigma^{res}_{XX}(Y, Z)\mathrm{d}Y \tag{18}$$

9. First results

In this section several numerical simulations have been performed. The influence of three coiling parameters have been tested namely: applied forces, strip geometrical profiles and mandrel's radii. Parameters are listed in Table 2 and the tested parameters are listed in Table 4. For each test five cycles are modeled and results for the fifth wrap are presented in Figs. 16–18.

Test 1. Contact pressures, tangential stress and contact length increase when the applied force increases. Stresses keep the same distribution along the coil width (with a scale factor), so stresses do not localize, the increase being only due to the applied force. Thus the higher the stress peak is and the higher the contact length is. Plastic zones generated during step 2 are wider and wider when plastic deformations during step 1 do not evolve since the mandrel's radius is the same for all tested applied forces (thus the radius of curvature does not evolve much).

Test 2. The strip crown is increased by decreasing the thickness t_e at the edges of the strip. When there is no strip crown (i.e., $t_e = t_c = 1$ mm) the contact is ensured all along the coil width. The strip crown is responsible for the barrel shape (i.e., the contact length decrease) as explained in the introduction, thus the more severe the crown is and the shorter the contact length is. Therefore contact pressure and tangential stress localize where the contact is ensured which explains that stress peaks are higher and higher. Plastic deformations during step 1 is similar to the test 1 since the radius of curvature does not evolve much. At the center of the coil where contact is ensured for all tests, plastic deformations during step 2 are also similar to the test 1. However, one can see in Figs. 16e and 17e that the evolution of the average residual stress through thickness defined by (18) have different profiles along the coil width if stresses localize at the center (test 2) or not (test 1).

Test 3. The contact pressure and tangential stress peaks increases when the mandrel's radius decreases. This is due to the fact that the contact length decreases so that pressures localize alike the test 2. Therefore plastic deformations where stresses concentrate present significant variations during step 2 but also in step 1 because the radius of curvature evolves significantly. For a mandrel's radius of 500 mm the curvature is not sufficient to generate plastic deformations. When the curvature increases for mandrel's radii of 300 mm and 100 mm plastic deformations during step 1 are more and more severe: plastic zones are larger and gradients are higher. But since contact pressure and tangential stress localize more and more at the center of the coil ($Z = 0$) plastic elongations during step 2 are also more and more severe with higher gradients. This gradient increase is due to the fact that at the end of step 1 larger plastic zones (i.e., a smaller elastic zone) are obtained for smaller mandrel's radii, thus the additional stress peak during step 2 is not only higher but also applied on a smaller elastic region. For tests 1 and 2 gradients of plastic deformations during step 2 are constant because the stress peak is applied on the same elastic region, plastic zones being larger and larger because of the stress peak increase.

10. Conclusion

This paper presents a coiling model taking into account elastic-plastic behavior at finite strain considering isotropic hardening. Multiplicative formalism is used as well as an additive correction under infinitesimal strain assumption. The modeling strategy involves a fully analytical solution (step 1) and a semi-analytical solution (step 2). The global simulation relies on several optimization problems in order to determine contact pressures and the radius of curvature that enables to match the tangential applied force. Roughness has been considered using composite Abbott curves and empirical laws. This part being an external input of the model, one can consider other options. Comparisons with already existing models have been addressed and good agreement is observed for large yield stress. However, for lower yield stress the numerical solution presents more discrepancies with purely elastic models found in the literature showing the interest of an elastic-plastic computation. A simple purely elastic uncoiling model has been

proposed in order to quantify residual stresses after unwinding and releasing tension. Results show that the coiling process can be responsible for significant residual stress fields due to plastic deformations. Since the model is based on analytical or semi-analytical sub-steps, reasonable computation times are obtained. For instance five cycles are computed within 1 min with the freeware Scilab (2012), where a classical FEM computation using explicit integration scheme (with stability issues) takes several weeks. However, computation times grow exponentially (due to larger optimization problems) and 70 cycles are computed within around 24 hours. The code should be optimized and re-written in a compiled language such as C++ in order to obtain shorter computation times.

Acknowledgment

Authors gratefully acknowledge Eliette Mathey (*ArcelorMittal Global Research & Development, Maizières Process, 57283 Maizières-lès-Metz, France*) for providing results of her Finite Element simulation of coiling process used in Section 6.2.

Appendix A. Analytical solution of step 2

Thus, let consider a plastic zone where the plastic mechanism 1 or 2 is activated, thus:

$$\max_{\alpha\in\{rr,\theta\theta,zz\}}\left(\sigma_\alpha^{(2)}+\sigma_\alpha^{(1)}\right)-\min_{\alpha\in\{rr,\theta\theta,zz\}}\left(\sigma_\alpha^{(2)}+\sigma_\alpha^{(1)}\right)$$
$$=\chi\left[\sigma_{\theta\theta}^{(2)}+\sigma_{\theta\theta}^{(1)}-\left(\sigma_{rr}^{(2)}+\sigma_{rr}^{(1)}\right)\right] \tag{A.1}$$

where $\chi=1$ if the mechanism 1 is activated and $\chi=-1$ if the mechanism 2 is activated. In these conditions, the Tresca yield function (10) vanishes and reduces to:

$$\sigma_{\theta\theta}^{(2)}-\sigma_{rr}^{(2)}=K(r)+\chi\sigma_0\gamma\Delta p_{cum} \tag{A.2}$$

where:

$$K(r)=\chi k(p_{cum})-\left(\sigma_{\theta\theta}^{(1)}-\sigma_{rr}^{(1)}\right) \tag{A.3}$$

It should be noted that $K(r)$ is known from *step 1*. Let $\underline{\boldsymbol{\varepsilon}}^{\,p}$ denote the plastic strain of *step 2*. At the beginning of this step, $\underline{\boldsymbol{\varepsilon}}^{p}=0$. The total plastic strain of both steps (1 and 2) is obtained by adding the plastic strain of *step 1* and the plastic strain of *step 2*. The flow rule is associated therefore the plastic strain rates are normal to the Tresca yield surface corresponding to this plastic mechanism, thus:

$$\dot\varepsilon_{\theta\theta}^{p}=-\dot\varepsilon_{rr}^{p}\quad\text{and}\quad\dot\varepsilon_{zz}^{p}=0 \tag{A.4}$$

Hence the cumulative plastic strain rate for this step:

$$\dot p_{cum}=\sqrt{\frac{2}{3}\left(\left[\dot\varepsilon_{rr}^{p}\right]^2+\left[\dot\varepsilon_{\theta\theta}^{p}\right]^2+\left[\dot\varepsilon_{zz}^{p}\right]^2\right)}=\zeta\sqrt{\frac{4}{3}}\dot\varepsilon_{\theta\theta}^{p} \tag{A.5}$$

where ζ is the sign of $\dot\varepsilon_{\theta\theta}^{p}$. An initial guess is of course $\zeta=\chi$ which means that tangential plastic flow is positive when the strip is under tension. If displacement and normal stress continuity is not verified in the end the other value is set for ζ. After integration (considering that at the beginning of *step 2*, $\varepsilon_{\theta\theta}^{p}=0$):

$$\Delta p_{cum}=\zeta\sqrt{\frac{4}{3}}\varepsilon_{\theta\theta}^{p} \tag{A.6}$$

The equilibrium can be written as follows:

$$\frac{\mathrm{d}\sigma_{rr}^{(2)}}{\mathrm{d}r}+\frac{\sigma_{rr}^{(2)}}{r}-\frac{\sigma_{\theta\theta}^{(2)}}{r}=0 \tag{A.7}$$

Using the yield criterion (A.2), the latter equilibrium (A.7) reduces to:

$$\frac{\mathrm{d}\sigma_{rr}^{(2)}}{\mathrm{d}r}=\frac{K(r)}{r}+\chi\sigma_0\gamma\zeta\sqrt{\frac{4}{3}}\frac{\varepsilon_{\theta\theta}^{p}}{r} \tag{A.8}$$

Hence after integration:

$$\begin{cases}\sigma_{rr}^{(2)}=A+\displaystyle\int^r\frac{K(\rho)}{\rho}\mathrm{d}\rho+\chi\sigma_0\gamma\zeta\sqrt{\frac{4}{3}}\int^r\frac{\varepsilon_{\theta\theta}^{p}(\rho)}{\rho}\mathrm{d}\rho\\ \sigma_{\theta\theta}^{(2)}=A+\displaystyle\int^r\frac{K(\rho)}{\rho}\mathrm{d}\rho+\chi\sigma_0\gamma\zeta\sqrt{\frac{4}{3}}\int^r\frac{\varepsilon_{\theta\theta}^{p}(\rho)}{\rho}\mathrm{d}\rho\\ \qquad+K(r)+\chi\sigma_0\gamma\zeta\sqrt{\frac{4}{3}}\varepsilon_{\theta\theta}^{p}\end{cases} \tag{A.9}$$

The Cauchy stress tensor can be written as follows:

$$\begin{cases}\sigma_{rr}^{(2)}=\left(k_0+\frac{4\mu_0}{3}\right)\frac{\mathrm{d}u_r^{(2)}}{\mathrm{d}r}+\left(k_0-\frac{2\mu_0}{3}\right)\frac{u_r^{(2)}}{r}-2\mu_0\varepsilon_{rr}^{p}\\ \sigma_{\theta\theta}^{(2)}=\left(k_0-\frac{2\mu_0}{3}\right)\frac{\mathrm{d}u_r^{(2)}}{\mathrm{d}r}+\left(k_0+\frac{4\mu_0}{3}\right)\frac{u_r^{(2)}}{r}-2\mu_0\varepsilon_{\theta\theta}^{p}\\ \sigma_{zz}^{(2)}=\left(k_0-\frac{2\mu_0}{3}\right)\left(\frac{\mathrm{d}u_r^{(2)}}{\mathrm{d}r}+\frac{u_r^{(2)}}{r}\right)+2\mu_0\left(\varepsilon_{rr}^{p}+\varepsilon_{\theta\theta}^{p}\right)\end{cases} \tag{A.10}$$

The equilibrium (A.7) can be written using displacements in order to determine $\varepsilon_{\theta\theta}$:

$$\frac{\mathrm{d}}{\mathrm{d}r}\left[\frac{\mathrm{d}u_r^{(2)}}{\mathrm{d}r}+\frac{u_r^{(2)}}{r}\right]=\frac{2\mu_0}{k_0+\frac{4\mu_0}{3}}\left(\frac{\mathrm{d}\varepsilon_{rr}^{p}}{\mathrm{d}r}+\frac{\varepsilon_{rr}^{p}}{r}-\frac{\varepsilon_{\theta\theta}^{p}}{r}\right) \tag{A.11}$$

By integrating the flow rule (A.4), knowing that at the beginning of *step 2* the plastic strain tensor vanishes it is obtained:

$$\frac{\mathrm{d}}{\mathrm{d}r}\left[\frac{\mathrm{d}u_r^{(2)}}{\mathrm{d}r}+\frac{u_r^{(2)}}{r}\right]=-\frac{2\mu_0}{k_0+\frac{4\mu_0}{3}}\left(\frac{\mathrm{d}\varepsilon_{\theta\theta}^{p}}{\mathrm{d}r}+2\frac{\varepsilon_{\theta\theta}^{p}}{r}\right) \tag{A.12}$$

The following expression holds by adding the two first component of the Cauchy stress tensor (A.10):

$$\sigma_{rr}^{(2)}+\sigma_{\theta\theta}^{(2)}=2\left(k_0+\frac{\mu_0}{3}\right)\left(\frac{\mathrm{d}u_r^{(2)}}{\mathrm{d}r}+\frac{u_r^{(2)}}{r}\right) \tag{A.13}$$

Hence:

$$-\frac{4\mu_0\left(k_0+\frac{\mu_0}{3}\right)}{k_0+\frac{4\mu_0}{3}}\left(\frac{\mathrm{d}\varepsilon_{\theta\theta}^{p}}{\mathrm{d}r}+2\frac{\varepsilon_{\theta\theta}^{p}}{r}\right)=\frac{\mathrm{d}}{\mathrm{d}r}\left[\sigma_{rr}^{(2)}+\sigma_{\theta\theta}^{(2)}\right] \tag{A.14}$$

Using (A.9):

$$\frac{\mathrm{d}}{\mathrm{d}r}\left[\sigma_{rr}^{(2)}+\sigma_{\theta\theta}^{(2)}\right]=2\left(\frac{K(r)}{r}+\chi\sigma_0\gamma\zeta\sqrt{\frac{4}{3}}\frac{\varepsilon_{\theta\theta}^{p}}{r}\right)+\frac{\mathrm{d}K(r)}{\mathrm{d}r}$$
$$+\chi\sigma_0\gamma\zeta\sqrt{\frac{4}{3}}\frac{\mathrm{d}\varepsilon_{\theta\theta}^{p}}{\mathrm{d}r} \tag{A.15}$$

And:

$$\frac{\mathrm{d}\varepsilon_{\theta\theta}^{p}}{\mathrm{d}r}+2\frac{\varepsilon_{\theta\theta}^{p}}{r}=\xi\left(\frac{\mathrm{d}K(r)}{\mathrm{d}r}+2\frac{K(r)}{r}\right) \tag{A.16}$$

Where:

$$\xi=\frac{-1}{\frac{4\mu_0\left(k_0+\frac{\mu_0}{3}\right)}{k_0+\frac{4\mu_0}{3}}+\chi\sigma_0\gamma\zeta\sqrt{\frac{4}{3}}} \tag{A.17}$$

Hence:

$$\varepsilon_{\theta\theta}^{p}=\frac{B}{r^2}+\frac{\xi}{r^2}\int^r\rho^2\left(\frac{\mathrm{d}K(\rho)}{\mathrm{d}\rho}+2\frac{K(\rho)}{\rho}\right)\mathrm{d}\rho \tag{A.18}$$

Displacements are then determined by combining (A.13) and (A.9):

$$\frac{\mathrm{d}u_r}{\mathrm{d}r}+\frac{u_r}{r} = \frac{1}{2\left(k_0+\frac{\mu_0}{3}\right)}\left[2\left(A+\int^r\frac{K(\rho)}{\rho}\mathrm{d}\rho+\chi\sigma_0\gamma\zeta\sqrt{\frac{4}{3}}\int^r\frac{\varepsilon^p_{\theta\theta}(\rho)}{\rho}\mathrm{d}\rho\right) +K(r)+\chi\sigma_0\gamma\zeta\sqrt{\frac{4}{3}}\varepsilon^p_{\theta\theta}\right]=g(r) \tag{A.19}$$

Hence:

$$u_r=\frac{C}{r}+\frac{1}{r}\int^r\rho g(\rho)\mathrm{d}\rho \tag{A.20}$$

Analytical close form solution is obtained with (A.18) in combination with (A.20) and (A.9). However, a simpler formulation is needed for the practical implementation. Using the piece-wise polynomials interpolation (13) the displacement, strain and stress fields (14) are obtained after basic calculations.

Appendix B. Uncoiling analytical calculations

The hyper-elastic neo-hookean behavior considered in this paper (see Le Dang (2013) for more details) leads to:

$$\underline{\boldsymbol{\sigma}}^u=\frac{\mu_0}{J_u^{\frac{5}{3}}}\underline{\boldsymbol{E}}^u_0.{}^t\underline{\boldsymbol{E}}^u_0+\left(k_0(J_u-1)-\frac{\mu_0}{J_u^{\frac{5}{3}}}\frac{\mathrm{tr}\left(\underline{\boldsymbol{E}}^u_0.{}^t\underline{\boldsymbol{E}}^u_0\right)}{3}\right)\underline{\mathbf{1}} \tag{B.1}$$

Where $J_u=\det\left(\underline{\boldsymbol{E}}^u_0\right)$. Since $\underline{\boldsymbol{\sigma}}^u$ is known, one can determine $\underline{\boldsymbol{E}}^u_0.{}^t\underline{\boldsymbol{E}}^u_0$ easily by considering the spherical and deviatoric parts:

$$\underline{\boldsymbol{E}}^u_0.{}^t\underline{\boldsymbol{E}}^u_0=\frac{\mathrm{tr}\left(\underline{\boldsymbol{E}}^u_0.{}^t\underline{\boldsymbol{E}}^u_0\right)}{3}\underline{\mathbf{1}}+\underline{\mathbf{dev}}\left(\underline{\boldsymbol{E}}^u_0.{}^t\underline{\boldsymbol{E}}^u_0\right) \tag{B.2}$$

By considering the trace of (B.1) it is obtained:

$$J_u=\frac{\mathrm{tr}(\underline{\boldsymbol{\sigma}}^u)}{3k_0}+1 \tag{B.3}$$

By considering the deviatoric part of (B.1) it is obtained:

$$\underline{\mathbf{dev}}\left(\underline{\boldsymbol{E}}^u_0.{}^t\underline{\boldsymbol{E}}^u_0\right)=\frac{J_u^{\frac{5}{3}}}{\mu_0}\underline{\mathbf{dev}}(\underline{\boldsymbol{\sigma}}^u) \tag{B.4}$$

By considering the determinant of (B.1) it is obtained that $\mathrm{tr}\left(\underline{\boldsymbol{E}}^u_0.{}^t\underline{\boldsymbol{E}}^u_0\right)$ is the only real root of the following polynomial of degree 3:

$$Q^u(U)=\left(\frac{3J_u^{\frac{5}{3}}}{\mu_0}\right)^3\det(\underline{\mathbf{dev}}(\underline{\boldsymbol{\sigma}}^u))-27J_u^2 +\left(\frac{3J_u^{\frac{5}{3}}}{\mu_0}\right)^2\mathrm{tr}(\underline{\mathbf{com}}(\underline{\mathbf{dev}}(\underline{\boldsymbol{\sigma}}^u)))U+U^3 \tag{B.5}$$

Where $\underline{\mathbf{com}}(.)$ represents the adjugate matrix. Thus, $\underline{\mathbf{dev}}\left(\underline{\boldsymbol{E}}^u_0.{}^t\underline{\boldsymbol{E}}^u_0\right)$ and $\mathrm{tr}\left(\underline{\boldsymbol{E}}^u_0.{}^t\underline{\boldsymbol{E}}^u_0\right)$ are known from (B.4) and (B.5) hence $\underline{\boldsymbol{E}}^u_0.{}^t\underline{\boldsymbol{E}}^u_0$ known from (B.2) and denoted as follows:

$$\underline{\boldsymbol{E}}^u_0.{}^t\underline{\boldsymbol{E}}^u_0=A^u_{rr}\boldsymbol{e_r}\otimes\boldsymbol{e_r}+A^u_{\theta\theta}\boldsymbol{e_\theta}\otimes\boldsymbol{e_\theta}+A^u_{zz}\boldsymbol{e_z}\otimes\boldsymbol{e_z} \tag{B.6}$$

The inverse transformation gradient $\underline{\boldsymbol{F}}^{-1}$, defined in (Weisz-Patrault and Ehrlacher (2015)) and corresponding to the inverse of the curvature of step 1, is applied:

$$\underline{\boldsymbol{F}}^{-1}=-\frac{R(X)}{R(X)+Y}\boldsymbol{e_X}\otimes\boldsymbol{e_\theta}+\boldsymbol{e_Y}\otimes\boldsymbol{e_r}+\boldsymbol{e_Z}\otimes\boldsymbol{e_z} \tag{B.7}$$

The total gradient transformation $\underline{\boldsymbol{E}}^u$ of the uncoiling process is assumed to be purely elastic:

$$\underline{\boldsymbol{E}}^u=\underline{\boldsymbol{F}}^{-1}.\underline{\boldsymbol{E}}^u_0 \tag{B.8}$$

Hence:

$$\underline{\boldsymbol{E}}^u.{}^t\underline{\boldsymbol{E}}^u=\underline{\boldsymbol{F}}^{-1}.\underline{\boldsymbol{E}}^u_0.{}^t\underline{\boldsymbol{E}}^u_0.{}^t\underline{\boldsymbol{F}}^{-1}=\widetilde{J}_u^2A^u_{\theta\theta}\boldsymbol{e_X}\otimes\boldsymbol{e_X}+A^u_{rr}\boldsymbol{e_Y}\otimes\boldsymbol{e_Y}+A^u_{zz}\boldsymbol{e_Z}\otimes\boldsymbol{e_Z} \tag{B.9}$$

Where $\widetilde{J}_u=\det\left(\underline{\boldsymbol{F}}^{-1}\right)=\frac{R(X)}{R(X)+Y}$. Finally the stress field after uncoiling and releasing tension, which defines the residual stress field, is given by:

$$\underline{\boldsymbol{\sigma}}^{res}=\frac{\mu_0}{\left(J_u\widetilde{J}_u\right)^{\frac{5}{3}}}\underline{\boldsymbol{E}}^u.{}^t\underline{\boldsymbol{E}}^u+\left(k_0\left(J_u\widetilde{J}_u-1\right)-\frac{\mu_0}{\left(J_u\widetilde{J}_u\right)^{\frac{5}{3}}}\frac{\mathrm{tr}\left(\underline{\boldsymbol{E}}^u.{}^t\underline{\boldsymbol{E}}^u\right)}{3}\right)\underline{\mathbf{1}} \tag{B.10}$$

References

Abaqus. 6.7 User's manual. *Inc. and Dassault systemes*, 2007.

Abdelkhalek, S., Montmitonnet, P., Legrand, N., Buessler, P., 2011. Coupled approach for flatness prediction in cold rolling of thin strip. Int. J. Mech. Sci. 53, 661–675.

Altmann, H.C., 1968. Formulas for computing stresses in center-wound rolls. Tappi J. 51 (4), 176.

Antaluca, E., 2005. Contribution à l'étude des contacts élasto-plastiques: effet d'un chargement normal et tangentiel. Ph.D. thesis. Villeurbanne, INSA.

Ärölä, K., von Hertzen, R., 2007. Two-dimensional axisymmetric winding model for finite deformation. Comput. Mech. 40 (6), 933–947.

Bonn, R., Haupt, P., 1995. Exact solutions for large elastoplastic deformations of a thick-walled tube under internal pressure. Int. J. Plastic. 11 (1), 99–118.

Bree, J., 1967. Elastic-plastic behaviour of thin tubes subjected to internal pressure and intermittent high-heat fluxes with application to fast-nuclear-reactor fuel elements. J. Strain Anal. Eng. Des. 2 (3), 226–238.

Bree, J., 1989. Plastic deformation of a closed tube due to interaction of pressure stresses and cyclic thermal stresses. Int. J. Mech. Sci. 31 (11), 865–892.

Chang, W., Etsion, I., Bogy, D.B., 1987. An elastic-plastic model for the contact of rough surfaces. J. Tribol. 109 (2), 257–263.

Chatzigeorgiou, G., Charalambakis, N., Murat, F., 2009. Homogenization of a pressurized tube made of elastoplastic materials with discontinuous properties. Int. J. Solid. Struct. 46 (21), 3902–3913.

Chu, S.-C., 1972. A more rational approach to the problem of an elastoplastic thick--walled cylinder. J. Franklin Inst. 294 (1), 57–65.

Collette, C., Counhaye, C., Ponthot, J., 2000. Integration of roughness transfer into a cold rolling model. Rev. Metall. Cahiers d'Informations Techniques(France) 97 (7), 961–969.

Counhaye, C., 2000. Modélisation et contrôle industriel de la géométrie des aciers laminés à froid. Ph.D. thesis. Université de Liège.

Cuong, T.D., Tardif, N., Limam, A., 2015. Experimental and numerical modeling of flatness defects in strip cold rolling. Int. J. Solids Struct.

Durban, D., 1988. Finite straining of pressurized compressible elasto-plastic tubes. Int. J. Eng. Sci. 26 (9), 939–950.

Durban, D., Kubi, M., 1992. A general solution for the pressurized elastoplastic tube. J. Appl. Mech. 59 (1), 20–26.

Edwards, W., Boulton, G., 2001. The mystery of coil winding. In: 2001 Iron and Steel Exposition and AISE Annual Convention, pp. 2001–2017.

Eraslan, A.N., Akis, T., 2004. Deformation analysis of elastic-plastic two layer tubes subject to pressure: an analytical approach. Turkish J. Eng. Environ. Sci. 28 (4), 261–268.

Eraslan, A.N., Akis, T., 2006. Plane strain analytical solutions for a functionally graded elastic–plastic pressurized tube. Int. J. Pres. Ves. Pip. 83 (9), 635–644.

Gao, X.-L., 1993. An exact elasto-plastic solution for a closed-end thick-walled cylinder of elastic linear-hardening material with large strains. Int. J. Pres. Ves. Pip. 56 (3), 331–350.

Greenwood, J., Williamson, J., 1966. Contact of nominally flat surfaces. In: Proceedings of the Royal Society of London A: Mathematical, Physical and Engineering Sciences, 295. The Royal Society, pp. 300–319.

Hacquin, A., 1996. Modelisation thermo-mecanique tridimensionnelle du laminage: couplage bande-cylindres [3D thermomechanical modelling of rolling processes: coupling strip and rolls]. Ph.D. thesis. Cemef Ecole des Mines de Paris. In French.

Hinton, J.L., 2011. A Study on the Effects of Coil Wedge During Rewinding of Thin Gauge Metals. Ph.D. thesis. Wright State University.

Hinton, J.L., Malik, A.S., Grandhi, R.V., 2011. An airy function to rapidly predict stresses in wound metal strip having asymmetric thickness profile. Int. J. Mech. Sci. 53 (10), 827–838.

de Hoog, F., Yuen, W., Cozijnsen, M., 2007. An inverse solution for winding stresses in wound coils of non-linear orthotropic material. J. Mech. Eng. Sci. Proceedings of the Institution of Mechanical Engineers, Part C 221 (12), 1521–1531.

Hudzia, J., Ferrauto, F., Gevers, P., 1994. Stress calculation applied to a coil, and optimization of coiling tension. Cah. Inf. Tech. Rev. Metall. 91 (6), 937–943.

Jackson, R.L., Streator, J.L., 2006. A multi-scale model for contact between rough surfaces. Wear 261 (11), 1337–1347.

Jiang, Z., Tieu, A., 2001. Modeling of the rolling processes by a 3-D rigid plastic/visco-plastic finite element method with shifted ICCG method. Comput. Struct. 40, 79–2727.

Kedl, D., 1992. Using a two dimensional winding model to predict wound roll stresses that occur due to circumferential steps in core diameter or to cross-web caliper variation. In: Proceedings of the Second International Conference on Web Handling, pp. 99–112.

Kpogan, K., Potier-Ferry, M., 2014. Buckling of long thin plates under residual stresses with application to strip rolling. In: Key Engineering Materials, 611. Trans Tech Publ, pp. 221–230.

Le Dang, H., 2013. Modélisation simplifiée des processus de laminage [Simplified model of rolling process]. Ph.D. thesis. École des Ponts ParisTech. In french.

Lee, Y., Wickert, J., 2002. Stress field in finite width axisymmetric wound rolls. J. Appl. Mech. 69 (2), 130–138.

Legrand, N., Labbe, N., Weisz-Patrault, D., Ehrlacher, A., Horsky, J., Luks, T., 2012. Analysis of roll gap heat transfers in hot steel strip rolling through roll temperature sensors and heat transfer models. Key Eng. Mater. 504–506, 1043–1048. 10.4028/www.scientific.net/KEM.504-506.1043.

Legrand, N., Weisz-Patrault, D., Labbe, N., Ehrlacher, A., Luks, T., Horsky, J., 2013. Characterization of roll bite heat transfers in hot steel strip rolling and their influence on roll thermal fatigue degradation. Key Eng. Mater. 554–557, 1555–1569.

Liu, M., 2009. A nonlinear model of center-wound rolls incorporating refined boundary conditions. Comput. Struct. 87 (9), 552–563.

Montmitonnet, P., 2006. Hot and cold strip rolling processes. Comput. Method. Appl. Mech. Eng. 195, 6604–6625.

Muskhelishvili, N., 1953. Some basic problems of the mathematical theory of elasticity. Noordhoff International Publishing, Groningen. 2nd edition (1977).

Nakhoul, R., Montmitonnet, P., Legrand, N., 2014. Manifested flatness defect prediction in cold rolling of thin strips. Int. J. Mater. Form. 1–10.

Nakhoul, R., Montmitonnet, P., Potier-Ferry, M., 2015. Multi-scale method for modeling thin sheet buckling under residual stresses in the context of strip rolling. Int. J. Solids Struct.

Parker, A.P., 2001. Autofrettage of open-end tubes—pressures, stresses, strains, and code comparisons. J. Pres. Ves. Technol. 123 (3), 271–281.

Perry, J., Aboudi, J., 2003. Elasto-plastic stresses in thick walled cylinders. J. Pres. Ves. Technol. 125 (3), 248–252.

Polycarpou, A.A., Etsion, I., 1999. Analytical approximations in modeling contacting rough surfaces. J. Tribol. 121 (2), 234–239.

Pronina, Y., 2013. Analytical solution for the general mechanochemical corrosion of an ideal elastic–plastic thick-walled tube under pressure. Int. J. Solids Struct. 50 (22), 3626–3633.

Scilab, 2012. Scilab: Free and open source software for numerical computation. Scilab Enterprises, Orsay, France.

Sheu, S., Wilson, W.R., 1994. Mixed lubrication of strip rolling. Tribol. Trans. 37 (3), 483–493.

Sims, R., Place, J., 1953. The stresses in the reels of cold reduction mills. British J. Appl. Phys. 4 (7), 213.

Sutcliffe, M., 1988. Surface asperity deformation in metal forming processes. Int. J. Mech. Sci. 30 (11), 847–868.

Wadsley, A., Edwards, W., 1977. Coil winding stresses. J. Australas. Inst. Met. 22 (1), 17–27.

Weisz-Patrault, D., 2015. Inverse cauchy method with conformal mapping: application to latent flatness defect detection during rolling process. Int. J. Solids Struct. 56 (57), 175–193.

Weisz-Patrault, D., Ehrlacher, A., 2015. Curvature of an elasto-plastic strip at finite strains: application to fast simulation of coils. 22th Congrès Français de Mécanique. Association Française de Mécanique.

Weisz-Patrault, D., Ehrlacher, A., Legrand, N., 2011. A new sensor for the evaluation of contact stress by inverse analysis during steel strip rolling. J. Mater. Process. Technol. 211, 1500–1509. doi:10.1016/j.jmatprotec.2011.03.025.

Weisz-Patrault, D., Ehrlacher, A., Legrand, N., 2012a. Evaluation of temperature field and heat flux by inverse analysis during steel strip rolling. Inter. J. Heat Mass Transfer 55, 629–641. doi:10.1016/j.ijheatmasstransfer.2011.10.048.

Weisz-Patrault, D., Ehrlacher, A., Legrand, N., 2013a. Analytical inverse solution for coupled thermoelastic problem for the evaluation of contact stress during steel strip rolling. Appl. Math. Modell. 37, 2212–2229.

Weisz-Patrault, D., Ehrlacher, A., Legrand, N., 2013b. Evaluation of contact stress during rolling process, by three dimensional analytical inverse method. Int. J. Solids Struct. 50 (20–21), 3319–3331.

Weisz-Patrault, D., Ehrlacher, A., Legrand, N., 2014. Temperature and heat flux fast estimation during rolling process. Int. J. Thermal Sci. 75 (0), 1–20.

Weisz-Patrault, D., Ehrlacher, A., Legrand, N., Labbe, N., Horsky, J., Luks, T., 2012b. Experimental study of interfacial heat flux and surface temperature by inverse analysis with thermocouple (fully embedded) during hot steel strip rolling. Adv. Mater. Res. 452–453, 959–963. 10.4028/www.scientific.net/AMR.452-453.959.

Weisz-Patrault, D., Ehrlacher, A., Legrand, N., Mathey, E., 2015a. Non-linear numerical simulation of coiling by elastic finite strain model. Key Eng. Mater. 651–653, 1060–1065.

Weisz-Patrault, D., Maurin, L., Legrand, N., Salem, A.B., Bengrir, A.A., 2015b. Experimental evaluation of contact stress during cold rolling process with optical fiber bragg gratings sensors measurements and fast inverse method. J. Mater. Process. Technol. 223, 105–123.

Wilkening, H., 1965. Determination of the radial coiler loading during the coiling of strip. Rheinisch-Westfälischen Technischen Hochschule Aachen University Ph.D. thesis.

Wilson, W., Sheu, S., 1988. Real area of contact and boundary friction in metal forming. Int. J. Mech. Sci. 30 (7), 475–489.